Measuring gravitational wave memory with LISA

Henri Inchauspé [1,2,3,a] Silvia Gasparotto [4,5,b] Diego Blas [5,6]
Lavinia Heisenberg,[3] Jann Zosso [7,8] and Shubhanshu Tiwari[9]

[1] *Institute for Theoretical Physics, KU Leuven, Celestijnenlaan 200D, B-3001 Leuven, Belgium*
[2] *Leuven Gravity Institute, KU Leuven, Celestijnenlaan 200D box 2415, 3001 Leuven, Belgium*
[3] *Institut für Theoretische Physik, Universität Heidelberg, Philosophenweg 16, 69120 Heidelberg, Germany*
[4] *Grup de Física Teòrica, Departament de Física, Universitat Autònoma de Barcelona, 08193 Bellaterra (Barcelona), Spain*
[5] *Institut de Física d'Altes Energies (IFAE), The Barcelona Institute of Science and Technology (BIST), Campus UAB, 08193 Bellaterra, Barcelona*
[6] *Institució Catalana de Recerca i Estudis Avançats (ICREA), Passeig Lluís Companys 23, 08010 Barcelona, Spain*
[7] *Institute for Theoretical Physics, ETH Zurich, Wolfgang-Pauli-Strasse 27, CH-8093 Zurich, Switzerland*
[8] *Albert Einstein Center, Institute for Theoretical Physics, University of Bern, Sidlerstrasse 5, CH-3012 Bern, Switzerland*
[9] *Physik-Institut, Universität Zürich, Winterthurerstrasse 190, 8057 Zürich, Switzerland*

Gravitational wave (GW) astronomy has revolutionized our capacity to explore nature. The next generation of observatories, among which the space-borne detector Laser Interferometer Space Antenna LISA, is expected to yield orders of magnitude of signal-to-noise ratio improvement, and reach fainter and novel features of General Relativity. Among them, an exciting possibility is the detection of GW memory. Interpreted as a permanent deformation of the background spacetime after a GW perturbation has passed through the detector, GW memory offers a novel avenue to proof-test General Relativity, access the non-linear nature of gravity, and provide complementary information to better characterize the GW source. Previous studies have shown that GW memory detection from individual mergers of massive black hole binaries is expected with LISA. However, these works have not simulated the proper time domain response of the detector to the GW memory. This work is filling this gap and presents the detection prospects of LISA regarding GW memory and the expected signature of GW memory on the data-streams using the most up-to-date LISA consortium simulations of the response. We focus on the GW memory of massive black hole binary mergers and use state-of-the-art population models to assess the likelihood of detecting the GW memory within the LISA lifetime. We conclude that GW memory will be a key feature of several events detected by LISA, and will help to exploit the scientific potential of the mission fully.

I. INTRODUCTION

When an unbound flux of matter or radiation is released from a localized event, the final metric of the asymptotic region does not return to its original form, but the relative proper distances between freely falling observers are permanently modified with respect to their original ones. This phenomenon is called *gravitational wave memory* effect, see e.g. [1–4], or, in recent language, *displacement* memory, and is the dominant of several effects related to the changes of asymptotic states after the passage of radiation [5–10]. Remarkably, these effects are intimately connected to the asymptotic structure of space-time in General Relativity, namely with the symmetries of the BMS group [11–13], as well as the soft theorems [11, 14] in scattering theory.

In this work, we will focus on the GW memory generated by the passage of *gravitational flux*, known as *non-linear* memory to differentiate it from the *linear* memory, which is related to the unbound energy flux of other fields such as matter radiation or matter components.[1] Moreover, we will restrict to the *displacement* memory and not consider other subdominant effects, such as the *spin* [9] or the *center-of-mass* [10, 16] memories.

As the name suggests, the origin of such non-linear displacement memory stems from the non-linear nature of General Relativity: gravitational waves themselves carry energy-momentum that generates additional gravitational radiation, which precisely induces a displacement memory [4, 17–24]. Interestingly, GW memory is however no mere second order effect, but can be understood as a fundamental component of any gravitational radiation that reaches null infinity at leading order [4]. The relation of non-linear memory to the oscillatory *primary* GWs explains some of the features of the effect since its magnitude and its typical time scale, as well as its angular dependence are related to the flux emitted by

[a] henri.inchauspe@kuleuven.be
[b] sgasparotto@ifae.es

[1] Motivated by the BMS *balance laws* [12], Gravitational Wave (GW) memory is sometimes also categorized into so called *null* memory that represents memory that is sourced by any unbound null energy flux of radiation, and *ordinary* memory, associated to unbound energy-momentum of massive components that do not reach null infinity [15]. The non-linear memory of GR is therefore also part of the null memory.

the primary signal. However, memory nevertheless represents a unique non-linear effect that accumulates over time, whose non-oscillatory nature marks a clear distinction with the oscillatory primary waveform [22, 25]. As a result, the properties of the GW memory strongly differ from those of the primary waves and, despite only having a small imprint on typical interferometric GW detectors, memory may carry key complementary information from the primary signal. For instance, it may allow one to break the degeneracy between luminosity distance and inclination [26, 27] or between the merger of binary black holes or neutron stars [28, 29]. The use of GW memory has also been proposed to test the asymptotic symmetries of space-time [30], or as a part of consistency tests of waveform models exploiting balance laws [31, 32]. Furthermore, since GW memory probes the non-linear nature of gravitation, it is natural to expect changes in modified theories of gravity [33–36]. Finally, the different frequency span of the GW memory as compared to the primary signal allows looking for merger events at frequencies higher than the detector band [37] and even search for the same events in ground-base and space-borne detectors [38]. In conclusion, the detection of GW memory will open several possibilities to probe astrophysics and fundamental physics with GWs.

GW observations have so far not detected GW memory. This is mainly due to the smallness of the signal within current GW observatories and is true both for binary black hole coalescences observed in LIGO/Virgo data [39–42] and supermassive black hole coalescences that may explain Pulsar Timing Arrays data [43–45]. In fact, it is not expected for current ground-based interferometers to detect the memory from the coalescence of *individual* binary compact objects. Instead, it has been suggested that the combination of events with GW memory Signal-to-Noise Ratio (SNR) below threshold over 2 to 5 years may be enough to reach detection in these set-ups [7]. The prospects of detecting the memory from individual events are more promising for the next generation of detectors, either ground-based, such as the ET [46] and CE [47], and space-based interferometers like the Laser Interferometer Space Antenna (LISA) and TianQin [7, 26, 48–53] or SKA [54, 55].

In this paper, we focus on the characteristic imprint of the memory on the LISA detector from the coalescence of Massive Black Holes (MBHs) that merge in the frequency band between 10^{-4} Hz and 10^{-1} Hz. These events will have an extraordinarily high SNR, especially during the merger, when most of the memory is created. Consequently, these objects are the most promising source of detectable GW memory. Recent works [26, 52, 53] have confirmed that several MBH mergers will have an SNR of the GW memory sufficiently high to claim detection, though the expected number varies considerably depending on the astrophysical population considered. Building on these results, one of our main goals is to improve them by investigating the GW memory with the *full time-domain response of LISA*, based on Time Delay Interferometry (TDI) and its most updated noise characterization. Addressing the robustness of the detection of GW memory when TDI is considered is essential to build a solid understanding of the imprint of this effect, especially if one aims at using it as an additional source of information complementary to the leading oscillatory signal. We devote the rest of the paper to the first investigation in this direction for the LISA mission.

For the calculation of GW memory, we consider the `NRHybSur3dq8` waveform [56], which is one of the most accurate waveforms available to date, trained on numerical relativity simulations and including higher modes up to $\ell \leq 4$. This model has recently been updated to capture the GW memory `NRHybSur3dq8_CCE` [57], which for non-precessing binaries is mainly in the (2,0) mode [48]. This helps to perform consistency checks and to investigate the mixing of the memory and additional oscillatory features excited during the merger and ringdown, both of which are present in the (2,0) mode. We further perform a broad study of the parameter space of the binary merger by varying the mass ratio of the two black holes and the amplitude of the aligned spin of the sources, though we will not consider the presence of precession or non-trivial eccentricities. The detectability of GW memory by LISA will be assessed with state-of-the-art population models of MBHs described in Refs. [58, 59] (and based on previous work presented in [60–62]).

The paper is organized as follows. In Sec. II we describe the necessary tools for the subsequent analysis, such as the TDI processing, the LISA noise characterization and the waveform models. In Sec. III, we comprehensively describe how the displacement memory impacts the signal of LISA. In Sec. IV we discuss the signal-to-noise ratio and the detectability predictions. Sec. V is devoted to the study of MBHs mergers and the prospect of detecting memory from them in LISA. In Sec. VI, we explore the particular dependence of the memory SNR w.r.t. mass ratio and spin. Finally, we discuss our conclusions and outlook in Sec. VII.

II. DISPLACEMENT MEMORY IMPRINTS ON LISA INTERFEROMETRIC DATA

GW interferometers, either ground or space-based, are not designed to observe a permanent shift of the strain because they are sensitive to a limited frequency band. As a result, they cannot detect the permanent offset from the GW memory. However, the time-dependent transition in strain induced by the GW memory at the detector location does exhibit significant spectral content at low frequencies, which may be detected. Most of the MBH mergers in the LISA band, sensitive between 10^{-4}Hz and 10^{-1}Hz [63], will have a much higher SNR than events currently detected by ground-based interferometers, which allow the fine details of the waveform, such as the GW memory, to be distinguished. The proper determination of LISA's sensitivity to GW mem-

ory requires a full time-domain simulation of the projection of the signal onto the laser antenna response (down to TDI data streams). In this section, we show a comprehensive *end-to-end* time-domain simulation of the LISA response to the GW memory using the most up-to-date LISA consortium simulations (`LISAGWResponse` [64, 65], `LISAInstrument` [66, 67]) and post-processing software (`PyTDI` [68]).

A. GW memory model and simulation

1. Definition and computation of non-linear memory

To assess the detectability of the memory, it is important in a first step to provide a pertinent theoretical definition that allows to isolate it in the total GW strain. Focusing on non-linear memory, such a definition is given by the following integral over the energy flux emitted in primary GWs [17, 19, 22, 35][2]

$$\left[h_{ij}^{mem}\right]^{\rm TT} = \frac{4G}{Rc^4}\int_{-\infty}^{u} {\rm d}u' \int {\rm d}\Omega' \frac{{\rm d}E}{{\rm d}u'{\rm d}\Omega'}\left[\frac{n'_i n'_j}{1-n'_k N^k}\right]^{\rm TT}, \tag{1}$$

where u is the retarded time, R the luminosity distance of the detector to the source, $n' \equiv n(\Omega')$ are unit radial vectors centered at the source, $N \equiv n(\Omega)$ is the unit line-of-sight vector, and TT denotes a projection onto the TT-gauge along the relevant direction N [35, 70]. This formula describes a non-linear displacement memory component of the asymptotic radiation that is caused by any spherically asymmetric release of GW energy flux from a localized source. The characteristic angular dependence within the square brackets in Eq. (1) arises as a combination of the universal structure of any asymptotic energy-momentum tensor and the source-to-detector vector within the Green's function of the D'Alembert operator [23, 36]. Moreover, since the energy flux of GWs is integrated over the entire binary evolution, the GW memory is a *hereditary* effect. More precisely, it accumulates over time leaving an increasing off-set of the initial zero mean of the strain, leading to a non-zero geodesic deviation between any freely falling test-masses after the GWs have passed and therefore by definition induces a displacement memory effect. However, most of the effect comes from the merger stage, where about 5% of the total mass is released in GWs [71] which explains the characteristic step-like behaviour of the memory as seen in Figure 1.

[2] This formula explicitly does not capture any *linear* memory. A more general formula involving any type of unbound energy-momentum content can for instance be found in [36]. However, for binary black hole coalescence the only linear memory comes from a potential final black hole kick, which is a very subdominant contribution [69].

Fundamentally, the gauge-invariant energy flux of primary waves reads

$$\frac{{\rm d}E}{{\rm d}u'{\rm d}\Omega'} = \frac{R^2c^3}{16\pi G}\langle \dot{h}_{0+}^2 + \dot{h}_{0\times}^2\rangle, \tag{2}$$

where h_{0+} and $h_{0\times}$ are the amplitudes of the corresponding polarization states and the spacetime average $\langle ...\rangle$ is to ensure a well-defined energy content of GWs [35, 70, 72–74]. Such an average over the scales of variation of the GWs naturally arises within an Isaacson approach to defining GWs [75, 76], and in the context of memory, it allows for a clear distinction between so-called *primary waves*, defined as the oscillatory part of asymptotic radiation that we denote as h_0, and the non-linear memory that is fundamentally understood as a corresponding low-frequency correction [35]. However, for quasi-circular and non-precessing compact binary black hole coalescence, a special case which this work is restricted to, the spacetime average in (2) can effectively be dropped, as we explain in detail in App. A. It will therefore be ignored throughout this study. Nevertheless, is worth emphasizing that, as soon as eccentric or precessing binaries are considered, averaging over high-frequency scales becomes inevitable to define a memory signal clearly distinguishable from the primary wave. In the following, we therefore call the *memory signal* the part of the GW that is generated merely by the energy flux emitted in primary GWs.

It is useful to explicitly take into account the freedom in rotating the polarization basis of any outgoing radiation by defining the complex scalar

$$h \equiv h_+ - ih_\times, \tag{3}$$

with explicit spin-weight of $s=-2$ [77], that can therefore be expanded in terms of spin-weighted spherical harmonics

$$h(u,\Omega) = \sum_{\ell\geq 2}\sum_{|m|\leq\ell} h^{\ell m}(u)\,{}_{-2}Y_{\ell m}(\iota,\phi). \tag{4}$$

Projecting both the memory signal as well as the primary wave into the spin-weighted spherical harmonics basis, Eq. (1) can efficiently be evaluated, as the expansion helps to disentangle the angular and the time dependencies and yields a more compact representation of the angular dependence of the flux. Then, the angular integration in Eq. (1) can be performed either numerically as done by the `GWMemory` software (see Eq. (8) and (9) of [78]), or even analytically (see Eq. (A1) in the Appendix). From the analytical derivation, it can be seen that the memory is essentially showing up in the $(2,0)$ mode, since most of the primary GWs energy flux is released in the $(2,2)$ mode. More details are given in the App. A.

Throughout this work, we will therefore use the $(2,0)$ memory mode computed through the publicly available and numerically optimized `GWMemory` package with an input of primary waveforms from the surrogate model

NRHybSur3dq8 [56]. This surrogate model is the most accurate available for the parameter space of interest in this study (low mass-ratio q, focus on the merger). It is trained on numerical waveforms limited to mass-ratio $q < 8$ and spins aligned to the angular momentum of the binary with amplitude $\chi_{1,z}, \chi_{2,z} \in [-0.8, 0.8]$ (the model does not include precession or eccentricity).

2. *Alternative modeling approach*

The surrogate waveform model NRHybSur3dq8 [56] has recently been updated with NRHybSur3dq8_CCE [57], which is the first waveform model to include the full $(2,0)$ memory mode. These waveforms are calibrated to Numerical Relativity (NR) simulations that use a novel waveform extraction scheme called Cauchy-Characteristic Evolution (CCE) [13, 79], which directly captures the full low-frequency memory contribution. However, it is important to note that the $(2,0)$ mode does not purely capture the memory signal, but also includes oscillatory contributions excited during the ringdown, which are present in both the NRHybSur3dq8 and NRHybSur3dq8_CCE waveforms (see also App. C for further discussion).

Yet, with these two surrogate waveform models at hand, an alternative modelling approach for the memory within the $(2,0)$ mode can be envisaged by simply subtracting the oscillatory part present in NRHybSur3dq8 from the full mode in NRHybSur3dq8_CCE that contains the memory

$$h_+^{mem}(t) \equiv h_+^{(20)|cce}(t) - h_+^{(20)}(t). \tag{5}$$

This separation is shown in Figure 1, where we show the total waveform (blue) and the $(2,0)$ mode from the NRHybSur3dq8_CCE model (orange) and from the NRHybSur3dq8 (green) for a merger event with parameters $[M_{tot} = 10^6\ M_\odot,\ z = 1.0,\ q = 1.0,\ \iota = 1.047\,\text{rad},\ S = 0.0]$. From Figure 1, it becomes clear that Eq. (5) (grey-dashed) indeed allows us to isolate the memory from the oscillatory features of the ringdown in the $(2,0)$ mode.

In Figure 1 we also compare the memory model defined in Eq. (5) with the direct theoretical prediction in Eq. (1) computed by the GWMemory package (red). The two memory templates look similar, and yield comparable signal-to-noise ratios for equal-mass systems. However, a closer examination reveals sensible differences, and those are particularly pronounced for high-mass-ratio systems. The origin of this discrepancy is not entirely elucidated. It is suspected that different gauge fixing options taken by NRHybSur3dq8 and NRHybSur3dq8_CCE, related to the different strain extraction at null infinity strategies [57], make the direct comparison in Eq. (5) not well defined in general and especially for higher mass ratios q. This discrepancy will be investigated empirically, and the results of the comparison between Eq. (5) and GWMemory calculations will be presented in detail in App. C, as a by-product of this work.

Because of these uncertainties in isolating the memory model based on NR simulations, as opposed to the clear understanding of memory from Eq. (1), we will use the memory computed by the GWMemory package [78] throughout this work. This choice is also justified because the memory computed by Eq. (1) gives more conservative estimates in terms of SNR and smooth behaviour over the parameter space. It is emphasized that we are here focusing on the detectability of the memory only, as opposed to that of the entire $(2,0)$ mode, to which the oscillatory contribution from the ringdown adds significantly. We note that a phenomenological waveform model for the $(2,0)$ mode that includes both the memory and ringdown components has recently been implemented as an extension of the computationally efficient IMRPhenomTHM model [80] for the similar parameter space covered by NRHybSur3dq8, though without restriction on the length of the waveform. Once published, this can be used in the future for extensive Bayesian parameter estimation, which is currently very computationally expensive.

B. Detector response simulation

The simulation of the detector response requires the projection of the strain time-series computed in Section II A onto the space antenna response. For this, one first computes the interferometer's six single-link time-domain responses to the memory strain time-series using LISAGWResponse [64, 65]. This yields 6 time-series of relative (Doppler) frequency modulation $y(t) = \frac{\delta\nu}{\bar{\nu}}(t)$ of the laser link frequency caused by the GW crossing over the laser beam path:

$$y_{ij} = \frac{1}{2}\frac{\epsilon^a\epsilon^b}{1-\vec{\epsilon}\cdot\vec{k}}\left[h_{ab}\left(ct_r - \vec{k}\cdot\vec{x}_r\right) - h_{ab}\left(ct_e - \vec{k}\cdot\vec{x}_e\right)\right]. \tag{6}$$

Eq. (6) is called the two-pulse response [81] for the variable $y_{ij}(t)$, which is the relative Doppler shift time series observed from a vertex i of LISA between the local, emitted frequency ν_{ij} and the received distant laser frequency ν_{ji}. The latter frequency is subject to space-time geometry fluctuations as it travels along $\vec{\epsilon} \equiv \vec{\epsilon}_{j\to i}$ direction across the optical arm. The relative frequency fluctuation $y_{ij}(t)$ is reduced to the difference between the GW strain h_{ab} evaluated at the time of emission $(t_e, \vec{x}_e)$ and reception $(t_r, \vec{x}_r)$. Consequently, for GW wavelengths much larger than the constellation arm length L, $y \propto \dot{h}$ and the response in Eq. (6) behaves as a first order time differentiator. A comprehensive derivation of the time-domain link response can be found in App. A of Ref. [82].

The single-link frequency fluctuation data streams $y(t)$ are then injected into the PyTDI software [68] to simulate the virtual interferometer (i.e. suppressing primary noises, such as laser [64] and spacecraft jitter noise [83]). This generates the ultimate 3 interferometer time-series, selecting the A, E and T (second generation) variables

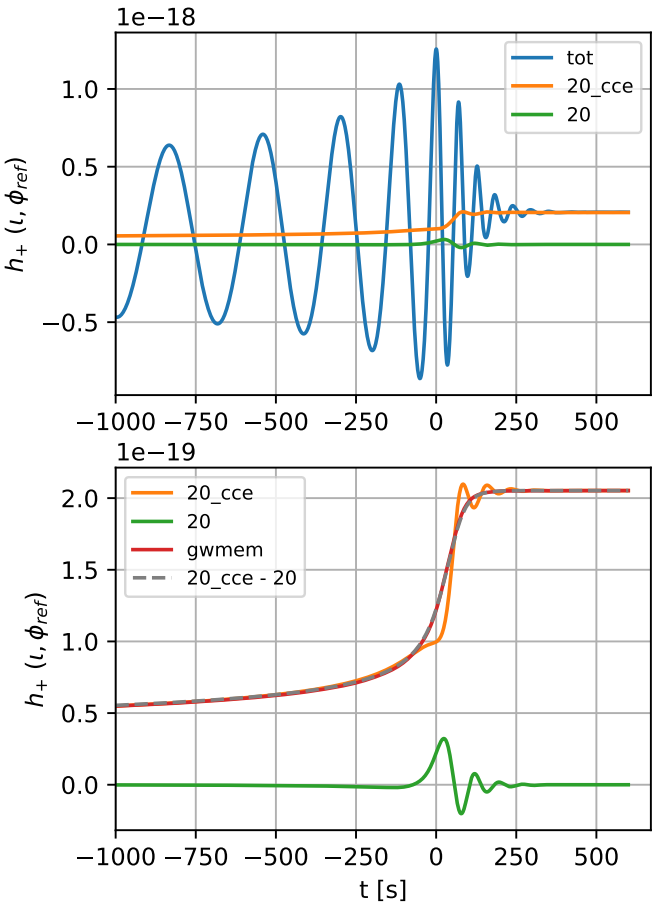

Figure 1. Breakdown of the oscillatory and memory component of the waveform from a $M_{tot} = 10^6 M_\odot$ MBHB merger. On the top plot: the total waveform (blue), the $(l, m) = (2, 0)$ component from `NRHybSur3dq8_CCE` (orange) and `NRHybSur3dq8` (green) models. On the bottom plot: a zoom-in on the `NRHybSur3dq8_CCE` model (orange) and the estimated contribution from GW memory (grey-dashed) according to Eq. (5), together with a comparison to the $(2, 0)$ mode computed with the `GWMemory` package [78] (red).

[81, 84] to work with nearly independent channels and ignoring residual cross-correlations, a sufficient set-up for SNR computations (more details about this are given in Section II C). Second-generation is needed to account for constellation flexing during the laser beam propagation time in the virtual interferometers, and then to suppress effectively laser noise below minimum requirements [85]. However, this second generation TDI impacts LISA response to GW, and typically acts as a second order time differentiator again at low frequency, i.e. for $\lambda_{GW} \gg L$ [86]. Keplerian orbits are considered for the constellation spacecraft, both for the single-link response and the time delays in TDI post-processing.

In addition, we performed several processing adjustments to facilitate the computation of the SNR around the merger time. First, the time reception shift of the wave at the detector location is ignored (setting `sun_shift = False`). This is a parameter specific to `LISAGWResponse`, where the timing frame for the input strain time series is understood from the location of the Solar System Barycentric (SSB) reference frame barycentre, implying a propagation time until it reaches the space interferometer. This makes the merger time depend on the sky-localization of the source, adding unnecessary complications for our scope here. Second, the time origin was adapted so that the merger time — defined as the time of the maximum $(l, m) = (2, 2)$ amplitude as conventional in literature [87] — is set to be $t_{\rm merger} = 0$. The time window width around $t = 0$ has been set to adapt dynamically to the total mass M_{tot} of the Massive Black Holes Binary (MBHB) system, ensuring to capture most of the oscillatory SNR for events with $M_{tot} > 10^5 M_\odot$, and to fully capture the memory SNR for all relevant MBHB masses $(10^4 M_\odot - 10^8 M_\odot)$. Finally, to avoid biases at low frequencies when representing the waveform in the frequency domain, especially occurring due to edge effects from the restricted time window and the GW memory step-like shape, we apply the Planck-taper window centred on the merger time, as extensively used in GW data analysis [88].

C. Noise settings

For the SNR determinations, LISA noise spectra are computed from single-link noise models, merely containing the two dominant secondary noises, i.e. the test mass (TM) acceleration noise and the Optical Metrology System (OMS) noise, and in agreement with the LISA Science Requirement Document (SciRD) [85],

$$S^{1/2}_{n|\rm TM} = 3 \times 10^{-15} \sqrt{\left[1 + \left(\frac{0.4\,\rm mHz}{f}\right)^2\right]\left[1 + \left(\frac{f}{8\,\rm mHz}\right)^4\right]}\ \frac{\rm m}{\rm s^2}\,\rm Hz^{-1/2}, \tag{7}$$

$$S^{1/2}_{n|\rm OMS} = 15 \times 10^{-12} \sqrt{\left[1 + \left(\frac{2\,\rm mHz}{f}\right)^4\right]}\ \rm m\,Hz^{-1/2}. \tag{8}$$

We then apply the TDI transfer function matrices on the single-link data streams based on the TDI-2 combi-

nations, defined as

$$X_2 = X_{1.5} + \mathbf{D}_{13121}y_{12} + \mathbf{D}_{131212}y_{21} + \mathbf{D}_{1312121}y_{13} + \mathbf{D}_{13121213}y_{31} - \big[\mathbf{D}_{12131}y_{13} + \mathbf{D}_{121313}y_{31} + \mathbf{D}_{1213131}y_{12} + \mathbf{D}_{12131312}y_{21}\big], \quad (9)$$

with

$$X_{1.5} = y_{13} + \mathbf{D}_{13}y_{31} + \mathbf{D}_{131}y_{12} + \mathbf{D}_{1312}y_{21} - (y_{12} + \mathbf{D}_{12}y_{21} + \mathbf{D}_{121}y_{13} + \mathbf{D}_{1213}y_{31}). \quad (10)$$

and where Y_2 and Z_2 can be deduced by circular permutation of the spacecraft indices $1 \to 2 \to 3 \to 1$. There, for example, y_{12} is the frequency modulation of the laser beam emitted by spacecraft 2 towards spacecraft 1, and as measured on spacecraft 1, then accumulating GW modulation along its path. $\mathbf{D}_{ij}$ is a delay operator which takes into account the light time travelled from one spacecraft i to the other j separated by the arm distance L_{ij}. In the frequency domain, the delay operator is a simple phase operator (Eq. (11)),

$$\mathbf{D}_{ij}x(t) = x(t - L_{ij}(t)) \xrightarrow{FT} \tilde{\mathbf{D}}_{ij}\tilde{x}(f) = \tilde{x}(f)\, e^{-2\pi i f L_{ij}(t)} \quad (11)$$

and $\mathbf{D}_{ijk\ldots}$ are nested time-delay operators. For example, the second term of Eq. (9), $\mathbf{D}_{13121} = \mathbf{D}_{13}\mathbf{D}_{31}\mathbf{D}_{12}\mathbf{D}_{21}$, is the time-domain operator used to delay the single-link data y_{12} by a time shift equal to the light travel time $L_{13121}(t)$ of a laser beam circulating across the spacecraft constellation, starting at spacecraft 1, making a round trip along arm 21, then going for a second round trip along 31 arm to finally ending back at spacecraft 1.
Arranging the TDI operators as a matrix applied on the single-link noise spectra as in [82], one gets the TDI-XYZ noise cross spectral density 3×3 matrix S_{XYZ}:

$$S_{XYZ}(f) = \mathbf{M}^{\mathrm{TDI}}(f)\; S_{ij}(f)\; \mathbf{M}^{\mathrm{TDI},\dagger}(f). \quad (12)$$

Converting to TDI-AET channels by a simple change of basis [89], one can get the A, E, T noise spectra:

$$S_{AET} = \begin{pmatrix} -\frac{1}{\sqrt{2}} & 0 & \frac{1}{\sqrt{2}} \\ \frac{1}{\sqrt{6}} & -\frac{2}{\sqrt{6}} & \frac{1}{\sqrt{6}} \\ \frac{1}{\sqrt{3}} & \frac{1}{\sqrt{3}} & \frac{1}{\sqrt{3}} \end{pmatrix} S_{XYZ}. \quad (13)$$

We assume S_{AET} to be diagonal to first approximation, as rotating TDI from XYZ to AET basis makes the noise to be nearly uncorrelated. Such property is exact for symmetric performances of X, Y and Z channels only [3]. However, we account for unequal arm constellation orbits in the modeling of S_{AA}, S_{EE} and S_{TT} diagonal elements for improved accuracy of the noise power spectrum models.
In addition to instrumental noise, we add for completeness a 4-years galactic confusion noise spectrum, equivalent to the residual power left by the unresolved (and non-extracted) GWs from galactic binaries after a 4-years observation run (minimal expected mission duration) [85, 90]. Finally, it is worth noting that the noise power spectrum required a smoothing treatment at the zero-response frequencies to counteract numerical instabilities when computing the SNR. Processing the single-link noise spectrum, we have considered multiple TDI transfer functions evaluated at 20 distinct epochs of the year and averaged the outputs to get the finally used TDI noise power spectrum. The procedure then provides a year-averaged power spectrum, as well as smoothed-out resonances, which now have a negligible impact on the SNR values.

We finally define the SNR of the primary and memory signals in LISA data as [86]:

$$\rho_C^2 = 4\,\mathrm{Re}\int_{f_{\min}}^{f_{\max}} \frac{\tilde{d}(f)\tilde{d}^*(f)}{S_{CC}(f)}\mathrm{d}f, \quad (14)$$

where $\tilde{d}(f)$ is the Fourier transform of an interferometer output channel $C \in \{A, E, T\}$ and all the spectra are *one-sided*. We combine the 3 TDI channels $C \in \{A, E, T\}$ summing the individual SNR ρ_C quadratically:

$$\rho_{\mathrm{tot}} = \sqrt{\sum_{C\in\{A,E,T\}} \rho_C^2}, \quad (15)$$

using the property of A, E and T channels of being approximately independent. Limited frequency range with $f_{\min} = 5 \times 10^{-5}$ Hz and $f_{\max} = 10^{-1}$ Hz is considered in the computation of ρ_{tot}, making sure that all the memory SNR and most of the $(2, 2)$ mode are captured, for any masses ranging from $10^4\, M_\odot$ to $10^8\, M_\odot$.

III. MEMORY SIGNATURE IN LISA DATA

Equipped with the above state-of-the-art simulation tools for the LISA TDI time-domain response to GW, we can now study the projection of the wave strain, defined as the $(2, 2)$ mode, and of the memory strain, defined as the memory component of the $(2, 0)$ mode explained above. This is shown for the three different channels A, E and T in Figure 2 for the GW of the same event considered in Figure 1. In the background of the same figure, and attached to the additional right-hand y-axis, we trace the $(2, 2)$ mode (down-scaled by $\times 0.05$) and the memory strain for a timing reference; the merger time is also indicated with a black dotted line. One observes from Figure 2 that the instrument response function acts as a high-pass filter for the memory signal, significantly reducing the overall amplitude and exhibiting time oscillations. In fact, at low frequency, i.e. for wavelengths

[3] the TDI-AET basis diagonalizes the cross-correlation matrix S_{XYZ} in case of a constellation symmetric over spacecraft cyclic permutation.

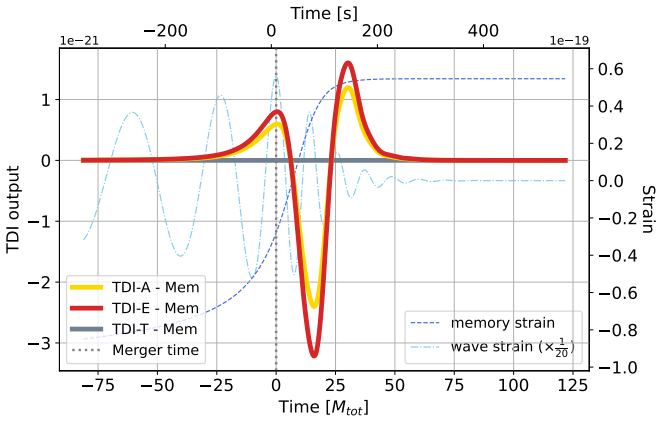

Figure 2. GW memory imprint of a binary merger with parameters $[M_{tot} = 10^6\ M_\odot, z = 1.0, q = 1.0, \iota = 1.047\,\text{rad}, S = 0.0]$ observed at sky latitude and longitude $[\beta = 0.52\text{rad}, \lambda = 3.24\text{rad}]$, on TDI time series A, E and T (resp. yellow, red and blue plain traces). The GW memory burst time-series as well as the sourcing oscillatory waveform strain ($\times 0.05$ down-scaled in amplitude) are superimposed in dashed-lines for timing and shape reference. Left Y-axis provides units for the TDI A, E and T channels (plain lines) while right Y-axis units are attached to the strain atime-series (dashed-lines). The merger time ($t = 0$) is indicated with a vertical dot-line.

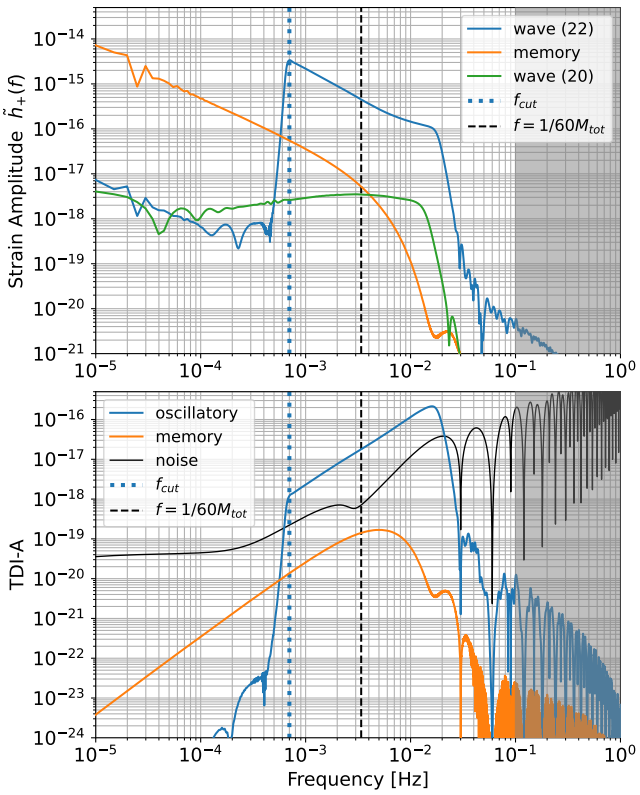

Figure 3. Up: Spectrum of the strain time-series $h_+(t)$, the wave $(l, m) = (2, 2)$ mode in blue, the wave $(l, m) = (2, 0)$ mode in green, and the memory in orange. Down: TDI-X time-series response to the wave $(l, m) = (2, 2)$ mode (in blue) and to the memory (in orange). The same system as in Figure 2, i.e. $[M_{tot} = 10^6\ M_\odot, z = 1.0, q = 1.0, \iota = 1.047\,\text{rad}, S = 0.0]$ is considered. The dashed gray lines on both figures mark the cut-off frequency applied at the inspiral due to computational time limitation (the oscillatory modes are invalid below that frequency. The gray frequency domains ($f < 5 \times 10^{-5}$Hz and $f > 10^{-1}$Hz) are excluded from the SNR computation.

longer than the arm length, the instrument response behaves as a high order differentiator [91]. As a result, the TDI output for the memory is mostly determined by $\partial_t^3 h$, as we show in Appendix B.

This can also be seen in the frequency domain in Figure 3, where we compare the spectra of the injected signals (up) and of the TDI outputs (down). The Fourier Transform (FT) of the memory on the upper panel (orange) scales as $1/f$ at low frequency and it decays at frequencies $f \gtrsim 1/60\,M_z$ where $M_z = (1 + z)M_{tot}$ is the redshifted total mass of the binary. This follows from the fact that, on time scales longer than its rising time, the memory is well approximated by a step-like function around the merger time, whose FT is $\sim 1/f$. At high frequency, the cutoff frequency is given by the duration of the memory saturation $\tau \sim 60\,M_z$, that corresponds to the time window around the merger, during which most of the GW energy $E_{\rm GW}$ is radiated [92].

We also show in Figure 3 the oscillating component of the $(2, 0)$ mode (green). It is interesting to note that the frequency $f = (60M_z)^{-1}$ (black dashed) represents a good transition above which this oscillatory component overcomes the memory. Again, this is consistent with identifying the pure memory with the low-frequency signal of the $(2, 0)$ mode. On the lower panel of Figure 3, we show the spectra of the TDI response to the (2,2) and memory modes of the waveform. Comparing the upper and lower subplots, focusing on the low-frequency *memory* spectra, we confirm the $\sim f^3(1/f)$ behavior of the LISA response which, in the long wavelength regime, manifestly approximates as a third-order time differentiator.

We stress that, to recover the expected spectrum of the memory strain shown in the upper panel of Figure 3, some processing of the waveform is needed that is different from the usual one applied to the oscillating wave. In particular, to recover the low-frequency behavior of the memory, we pad the strain to its final value for a sufficiently long time after the end of the generated waveform and use a Planck-taper window function to put the final value gradually to zero. This last step is crucial: otherwise, spectral leaking would completely spoil the weak signal from the memory. The issue of correctly processing the memory has also recently been discussed in [93], where an alternative method to recover a clean spectrum is proposed. However, we found that this issue is not present in the TDI output of the memory shown on the lower panel of Figure 2, since effectively the TDI output is proportional to higher derivatives of the injected signal

and the time series naturally goes to zero at the edges.

Further insight into the characterization of the memory in the data is provided by the time-frequency plot of the TDI signals of the primary wave and the memory. As shown in Figure 4, the two signals present a different localization in the time-frequency representation, with the (2,2) mode exhibiting the well-known *chirp* transient signal, increasing in power towards high frequencies, while the memory is confined to the merger time and relatively spread over frequencies, although with a maximum power frequency distinct from the (2,2) merger frequency.

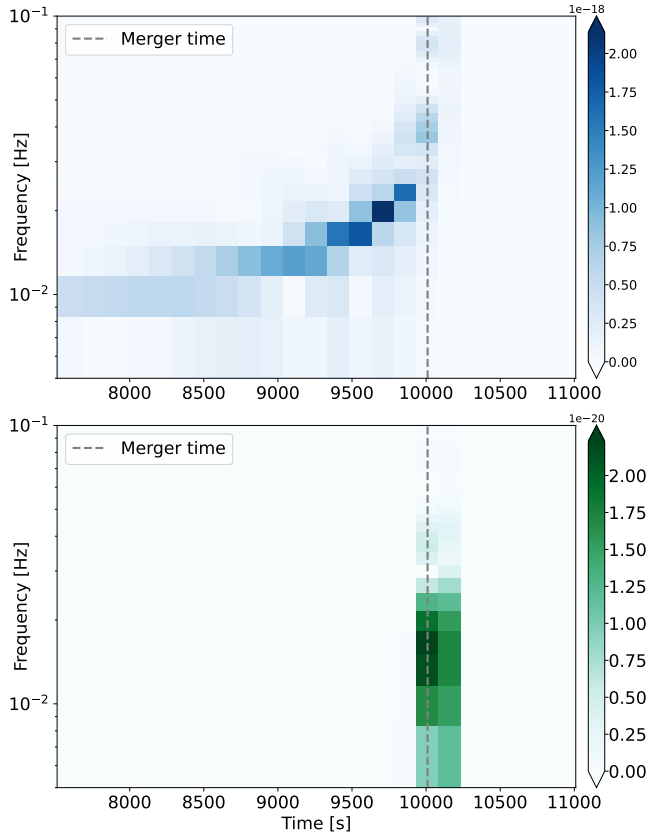

Figure 4. Spectrograms (short-time Fourier transforms) of the TDI-A signals from the GW (2,2) mode (top) and from the GW memory component (bottom) of an equal-mass system with total mass $M_{tot} = 10^5 M_\odot$. The two signals present a distinct localization in time-frequency representation, the (2,2) mode exhibiting the well-known *chirp* transient signal, increasing power towards high frequencies, whereas the memory is confined to merger time and relatively spread over frequencies, though with a maximum power frequency distinct from the (2,2) merger frequency. This representation provides helpful insight regarding strategies to identify memory from the main GW modes.

IV. SIGNAL-TO-NOISE RATIO AND DETECTABILITY PREDICTIONS

We begin by examining the SNR of the primary wave and the memory as a function of sky position, which is important for two main reasons: first, to study the potential improvement in sky localization from the information encoded in the memory; second, to understand its effect on the calculation of SNR. LISA will have a different relative sensitivity for the memory and the primary wave depending on the sky localization, as the antenna response function is frequency-dependent [95]. This could help better characterize the source signal's direction, especially for short signals, similar to what is found for the inclination angle in [26]. In addition, the direction of the source in the sky will primarily affect the SNR of the memory, which is more of a burst-like event, whereas since the main signal will be in the band for longer, the motion of the detector will average out the effects of localization.

We show an example of a sky-dependent map of the SNR for the primary wave, the memory, and their ratio, respectively, in Figure 5 for a binary's merger with parameters $M_{tot} = 10^6 M_\odot$, $z = 1.0$, $q = 2.5$, zero spin and inclination $\iota = 1.047$ (*conservative baseline* 1 in Table I). As expected, we find differences in the sky pattern between the primary and memory signals, captured by the different SNR ratios. Furthermore, we confirm our expectation that the sky localization primarily affects the SNR of the memory, e.g. for this particular system we find a relative factor within sky locations of ~ 7.5 for the memory compared to ~ 3 for the primary. These values depend on the particular source we choose, and we expect this difference to be even greater for lighter binaries that stay longer in band. The yellow dots in Figure 5 indicate a sky direction with average SNR, while the red dots indicate the sky direction with maximum SNR. The first is considered for the *conservative baseline* for the detectability study of section V, while the second is considered for the *optimistic baseline* for sky position. Since the sky maps are frequency-dependent, the sky directions for maximum and average SNR change slightly for different masses. The baseline set in our analysis (see Table I) is selected so that conservative and optimal assumptions remain valid across the examined mass range, in other words we marginalize over the total mass.

We now examine the dependence on the mass and redshift of the binary black hole. The SNR results for the primary and memory signals as a function of MBHB mass and redshift are shown in Figures 6 for an average scenario (baseline 1 in Table I). Note that the peak of the SNR for the memory occurs at lower masses compared to that of the primary wave, due to the clear frequency separation of the two signals. This is reflected in the right panel of Figures 6, where we see that the relative SNR of memory, which is less than the percentage level for the conservative baseline, increases for masses $M_{tot} \leq 10^{5.5} M_\odot$. The frequency content of the *mem-*

Baseline	q	χ	inclination ι [rad]	lat. β [rad]	long. λ [rad]	pixel p
1. Conservative	2.5	0.0	1.047	0.62	0.20	145
2. Optimistic	1.0	0.0	1.571	0.52	3.24	192
3. Opt. & Spin.	1.0	0.8	1.571	0.52	3.24	192

Table I. Table listing the three baselines used in this work regarding the choice of relevant merger parameters, such as the binary mass ratio q, the effective aligned spin χ, the inclination of the source ι, the sky-position (given as longitude and latitude angles β and λ in the SSB frame, or equivalently, as a pixel index in the sky assuming a sky discretization with $N_{\rm side} = 8$ *RING* scheme via `healpy` [94]).

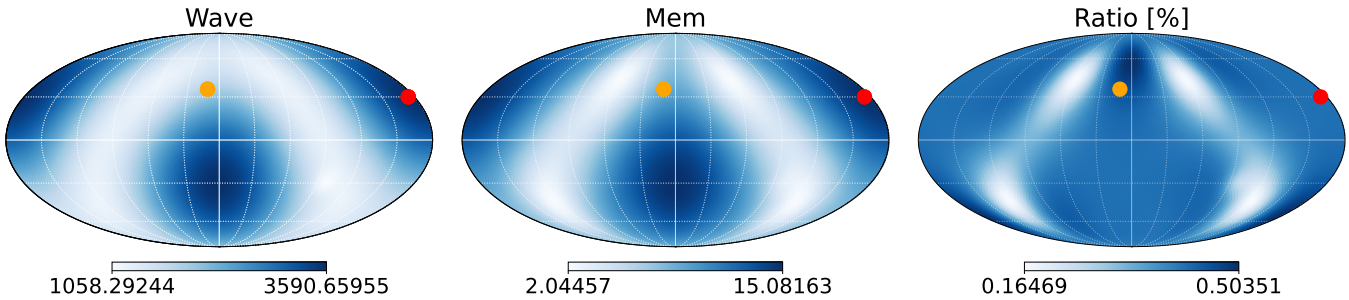

Figure 5. Sky-localization dependence of the GW (2,2) and memory modes SNR (resp. left and centre), and their ratio shown in percentage (right). The system studied here is a non-spinning $[M_{tot} = 10^6 M_\odot, q = 2.5, z = 1.0, \iota = 1.047\text{rad}]$ merger. The celestial sphere is decomposed into equal area pixels via the tool `healpy` [94, 96]), and the longitude λ and latitude β are converted into pixel indexes to be iterated over. We have sampled the sky into $N_{\rm pix} = 768$ pixels. The resulting sky map has been upsampled and smoothed spanning a Gaussian symmetry beam on the raw pixel data (see `smoothing` method from `healpy` [94, 96]). The yellow dots point to a sky-direction with average memory SNR used in baseline 1, while the red dot represents the optimal direction for memory SNR, which is considered in baseline 2 (see Table I).

ory signal indeed lands closer to LISA's high sensitivity spot for such lighter masses, hence the expectation of a greater effect in these cases.

In Figure 7, we show the same waterfall-type memory plots for the three different baselines of Table I: *conservative*, *optimistic*, and *optimistic with spins*. Note that the conservative and optimistic scenarios differ in sky location, inclination (median vs optimal), and also in the mass ratio ($q = 2.5$ vs $q = 1$). The optimal inclination for the memory is edge-on, since the $(2, 0)$ mode depends on the inclination angle as $(\sin\iota)^2$ [20], as opposed to the $(2, 2)$ mode, which is maximum for a face-on system. We will expand on the effect of the spin and the mass ratio in Section VI. Interestingly, the SNR can be enhanced by an order of magnitude for the same source which is relevant if one wants to use it to test General Relativity (which can be done with just a few loud events). We cross-checked our SNR results and found very good agreement with those presented in [97] for the primary wave and with those of [26] for the memory, where the SNR was computed in the frequency domain (without computing the TDI projection of the signal) and the antenna's pattern functions were averaged over the sky.

V. MBHS POPULATIONS AND DETECTABILITY PROSPECTS

With the results described in the previous sections, we are now in a position to study the number of mergers with detectable memory expected for LISA. To do this, we consider eight different astrophysical models of MBHBs mergers described in Refs. [58, 59], each of them considering a different choice for one of the main astrophysical uncertainties affecting the evolution of MBHs, which leads to rather different LISA event rates. The first uncertainty concerns the initial mass function for the "seeds" of the MBH population ["light seeds" (LS) of population III stars, or "heavy seeds" (HS) from the direct collapse of protogalactic gas disks], which primarily affects the final mass distribution of the population and thus the loudness of the mergers in the LISA band. Second, different time delays between the galaxy merger and the corresponding BBH mergers are considered: "delayed" models are more realistic and try to model processes at parsec distances (such as stellar hardening, triplet interactions, etc.); "short delays" neglect these and simply account for dynamical friction between halos. Since, for more realistic delays, the bulk of the mergers is shifted to lower redshifts, these models are the most promising ones in terms of detectability. Third, "SN" models include the effect of supernovae, which tends to inhibit the accretion of the MBH, so these models have lower final masses compared to "noSN" models.

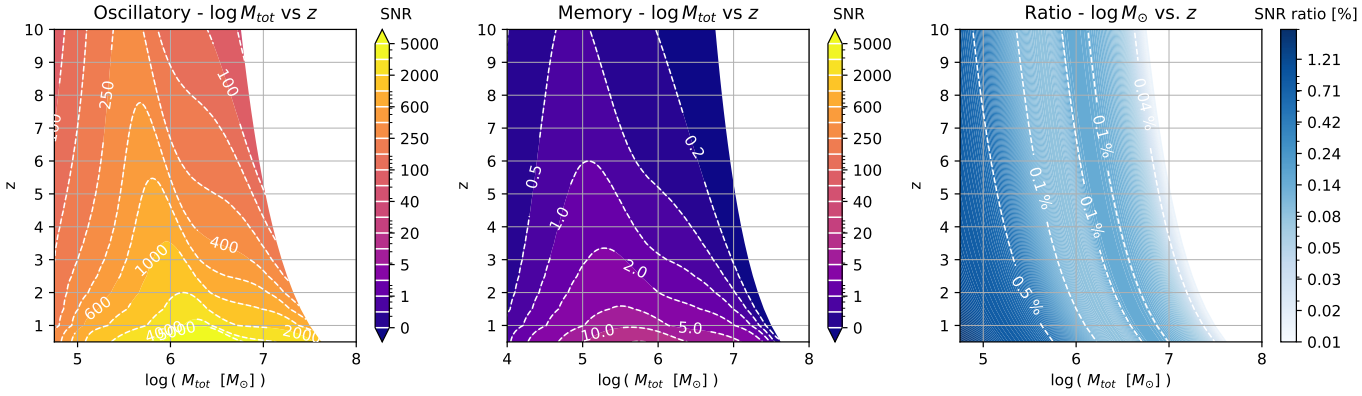

Figure 6. Contour plots of constant SNR lines for the primary wave *(left)*, the memory *(middle)* and the ratio between the SNR of the memory and that of the primary *(right)* considering the average scenario (baseline 1 described in Table I) for different MBHB merger systems.

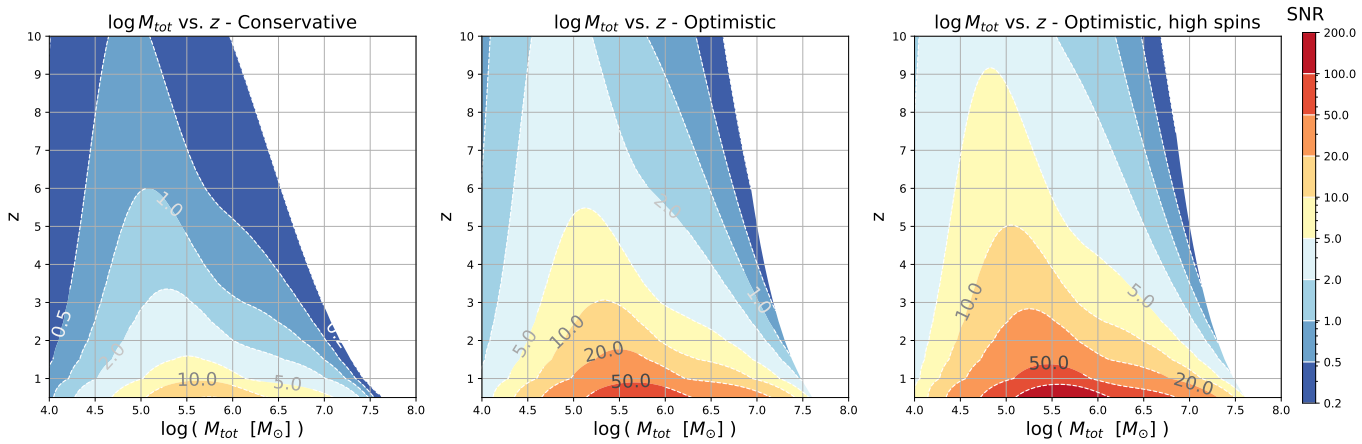

Figure 7. Contour plots for the constant SNR lines of the memory for the three baselines described in Table I, corresponding to different scenarios with increasing levels of optimism. *Left:* median inclination and sky location, mass ratio $q = 2.5$ and zero spin (baseline 1), *Middle:* optimal inclination and sky-position, $q = 1$ and zero spin (baseline 2), *Right:* optimal inclination and sky-position, $q = 1$ and $\chi_{1,z} = \chi_{2,z} = 0.8$ (baseline 3).

Our main results are presented in Figures 8 and 9 for the *conservative* and *optimistic* baselines of Table I, where we overlay the contour plots of the SNR to the contour plots of the number of mergers for the astrophysical populations in the mass-redshift plane, expected for 4 years of LISA observations. In the *conservative* scenario (cf. *baseline 1* in Table I), as in the previous section, we fix the sky direction corresponding to the average SNR, but for computing the waterfall-type plot we take the median of the distributions of the inclination ι and mass ratio q. The median is the middle value of the sample, so it tells us that half of the mergers will have a lower inclination (or mass ratio) and the other half a greater inclination (or mass ratio). If the direction of the angular momentum of the binary is random, then the inclination angle defined between $0 \leq \iota \leq \pi/2$ follows a $\cos(\iota)$ distribution[4] whose median is $\iota \approx 1.047$ rad. For the mass ratio, we find that, in all the different astrophysical populations considered, the median is $q \approx 2.5$, as opposed to the average value which varies for the different populations, since the mass ratio distributions are skewed and different, especially between the "heavy" and "light" seeds. The spin distributions are instead symmetric around zero. Therefore, the mean and the median are close to each other, and we consider no spin in the average scenario. In the *optimistic* scenario (cf. *baseline 2* in Table I), we consider an edge-on system with optimal sky-position, equal mass and zero spin.

As shown in Figures 8 and 9, the prediction for the number of events with detectable memory depends strongly on the astrophysical model considered. We con-

[4] A pedagogical explanation can be found in https://keatonb.github.io/archivers/uniforminclination.

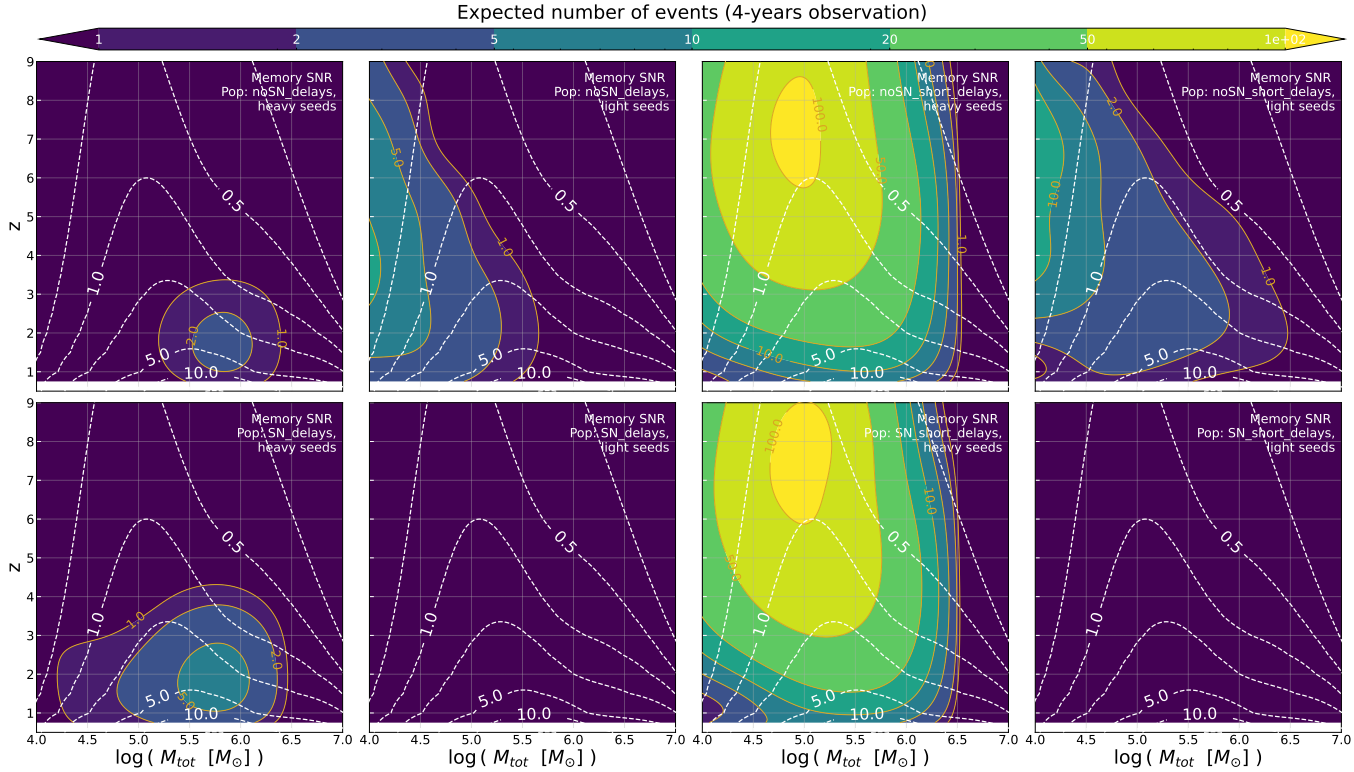

Figure 8. Overlay of the contours of the constant SNR of the memory for the *conservative* scenario (baseline 1) and the average number of mergers expected in 4 years for the different astrophysical population models described in [58, 59]. The first row shows the results for populations with SN feedback with "delays" or "short delays" for either the Heavy Seeds (HS) or the Light Seeds (LS). The second row is the same, but for populations without SN feedback.

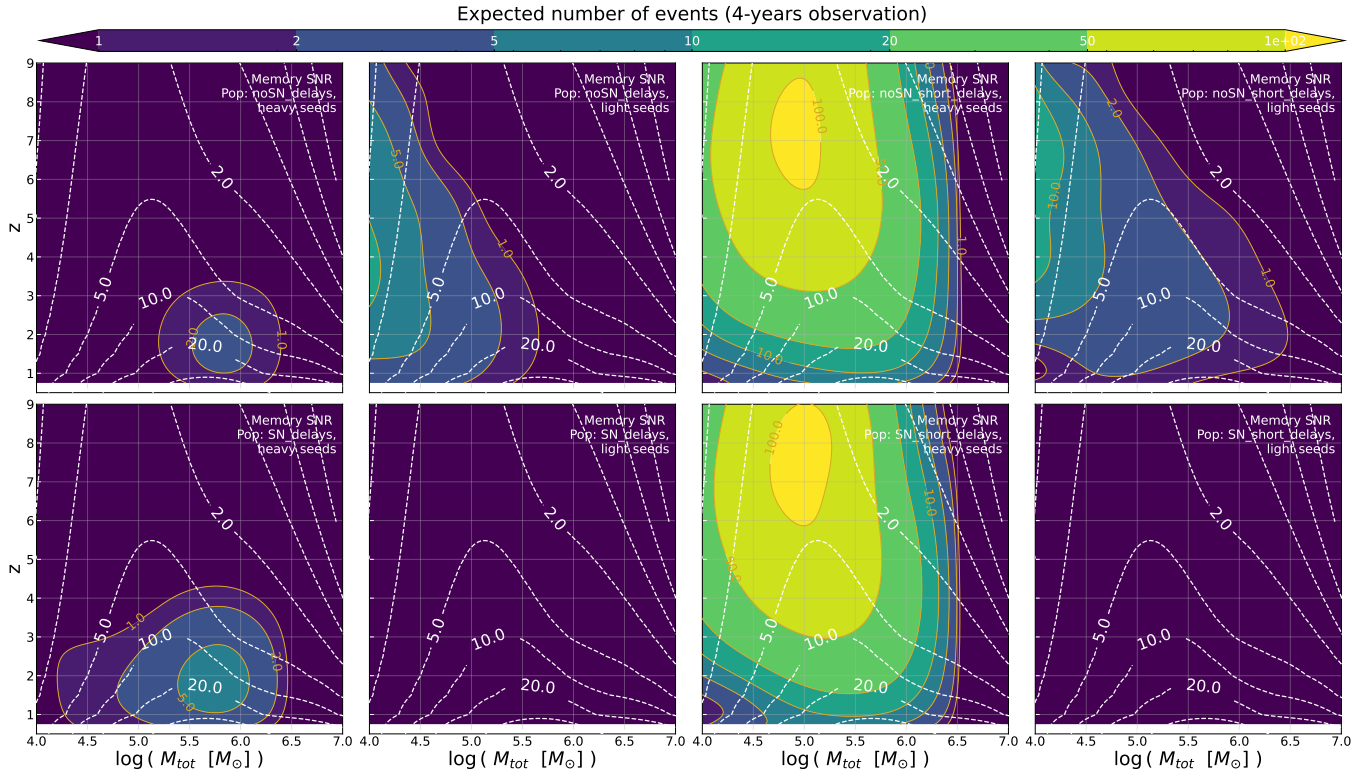

Figure 9. As Figure 8, but for the *optimistic* scenario (baseline 2).

firm previous results [26] that the most promising models are those starting with HS since, being the binaries more massive, the signals are louder. Among these HS models, the ones with short delays present many more events since the binaries start merging earlier, and we find no big effect of the SN feedback for those. On the other hand, the prospects are less promising for LS models, where the signals are weaker, and even less so for models with SN feedback, where the MBHs are lighter.

VI. MASS RATIO AND SPIN DEPENDENCE

In this section, we investigate the dependence of the SNR on the mass ratio and the total spin for different MBHs masses. The dependence of the memory on the mass ratio has been previously studied in [20, 41, 51, 78, 98], where it was shown that the final amplitude of the memory strongly decreases for asymmetric configurations. This trend is verified in Figure 10, showing SNR contours as a function of binary total masses M_{tot} and mass ratio q. The SNR peaks about $\log M_{tot} = 5.7$ and $q = 1$ and decreases monotonously with increasing values of q, while we recognize again in the horizontal behavior the frequency dependence of LISA sensitivity. On the lower panel of Figure 10, we show that the scaling of the memory SNR with the mass ratio q is approximated by $\sim [4q/(1+q)^2]^\alpha$ with $1 \leq \alpha \leq 2.5$, where $\alpha = 1$ is the Post-Newtonian expectation and $\alpha = 1.65$ was found in Ref. [98] for the final memory offset. We want to highlight that for light SMBHs, for which we expect a bigger impact of the memory on the total waveform, the memory decreases faster with mass ratio, strongly decreasing the possibility of detecting it far from the equal mass case. Instead, for higher total mass, the SNR scaling becomes less severe, because even if the amplitude of the signal decreases with q, the high-frequency cut-off of the memory shifts closer to the LISA high sensitivity frequency bins, hence mitigating the SNR loss.

The dependence of the memory on the spins was studied in [51, 98–100], where it was shown that the final amplitude of the memory increases monotonically with the symmetric spin $\chi_S = (m_1\chi_{1,z} + m_2\chi_{2,z})/M_{tot}$ and is independent of the antisymmetric combination $\chi_A = (m_1\chi_{1,z} - m_2\chi_{2,z})/2M_{tot}$, at least for the equal mass case. We confirm this dependence in Figure 11, where we compute the SNR of the memory for an equal mass case as a function of M_{tot} for different values of the individual spin, more precisely the spin component along the angular momentum $|\chi_{1,z}| = |\chi_{2,z}| = \chi$. As expected, the SNR of the memory just depends on the symmetric spin configuration, i.e. $\chi_{1,z} = \chi_{2,z} = \chi$, and has a maximum when the spins are aligned with the binary angular momentum. In this case, the SNR is about three times bigger than in the anti-aligned case. On the other hand, the memory SNR does not change when $\chi_{1,z} = -\chi_{2,z}$ since the symmetric spin is always zero for equal mass binary.

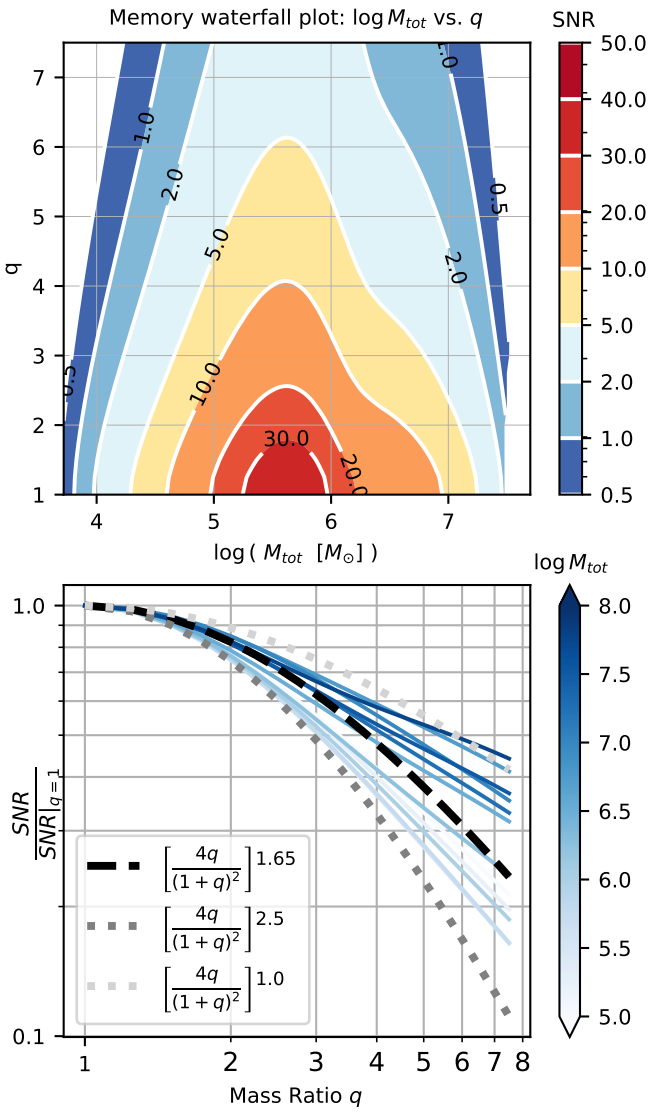

Figure 10. Study of the mass ratio dependence of the memory SNR, using the baseline 2 in Table I (apart from q obviously variable here). On the top panel: contour plot of the memory SNR as a function of total mass M_{tot} (x-axis) and mass ratio q (y-axis). On the lower panel: dependence of the SNR with the mass ratio q for a set of system total masses. This is compared with the scaling $\sim [4q/(1+q)^2]^\alpha$ with $1 \leq \alpha \leq 2.5$, where the $\alpha = 1$ is the Post-Newtonian expectation and $\alpha = 1.65$ was found in Ref. [98].

VII. DISCUSSION AND CONCLUSION

In this paper, we have extensively studied the imprint of gravitational (displacement) memory on the LISA detector. For the first time, we have simulated the TDI response of the detector to the passage of the GW memory contained in the (2,0) mode. As the LISA TDI response to the raw strain behaves as a third order differentiator, the memory signal appears as a burst-like event rather

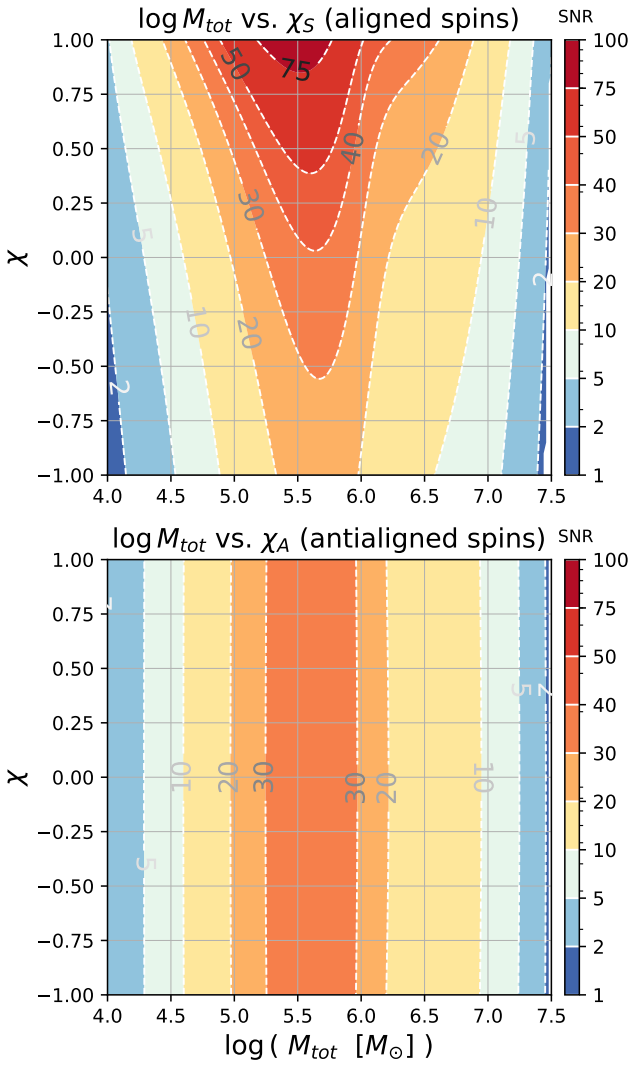

Figure 11. Study of the dependence of the memory SNR on the total amplitude of the spin for the aligned $\chi_{1,z} = \chi_{2,z} = \chi$ and anti-aligned $\chi_{1,z} = -\chi_{2,z}$ configurations. We use the baseline 2 in Table I (apart from χ variable here).

than a persistent offset. This burst-like behavior is evident in a time-frequency plot, where the memory signal becomes prominent just near the merger time. Therefore, a long waveform is not necessary to accurately calculate the memory SNR. Due to the shorter duration of the signal, the memory SNR is more dependent on the sensitivity of the detector to that particular direction of the sky, as opposed to longer signals where the effect of sky localization is averaged along the orbital motion of LISA. Indeed, we find that for MBHB mergers with different sky localizations, the memory SNR can vary by a factor of $\mathcal{O}(10)$. We then study the dependence of the memory SNR on the intrinsic parameters of the binary, such as mass and redshift, for three different scenarios with increasing levels of optimism *conservative*, *optimistic* and *optimistic with spin*, described in Table I.

We also compare the SNR results of eight different astrophysical populations of SMBHs to estimate the number of expected detectable sources and their parameter space distribution. Our results indicate that the detection prospects vary significantly with the population model, with heavy seeds models showing promising results and light seeds models yielding fewer detectable sources. Future work should explore these results further, especially for populations that better match the pulsar timing array signal as interpreted from the inspiral of SMBHs [101].

Data analysis issues regarding the extraction of GW memory signal from LISA TDI data will be an immediate extension of this work. The end-to-end time-domain simulation of the detection of the full Inspiral-Merger-Ringdown (IMR) waveform, including memory, is readily available for designing and testing data analysis strategies. Two approaches can be pursued. First, one can jointly fit the memory component, as computed from Eq. (1), together with the oscillatory component [102], hence evaluating the evidence of a memory signal detection (Bayes factor and hypothesis test). On the other hand, one can instead use an agnostic approach, combining a parameterized waveform model [102] together with a template-free time-frequency representation (e.g. wavelets), optimized for capturing low-frequency burst-like components such as the *memory signal*.

Other possible extensions of this project include investigating the effect of memory on binary parameter estimation and identifying regions of parameter space where neglecting memory leads to biases, similar to the analysis performed in [90] for higher harmonics. In addition, we could extend our study to subdominant memory components, such as *spin* memory. Our results are also relevant to the use of GW memory to perform consistency checks complementary to those performed with ringdown. Since the memory depends on the energy flux at infinity, it could potentially test additional radiation channels excited during the merger. Indeed, modified theories beyond General Relativity can affect the memory in both tensor perturbations of the metric and additional polarizations, as shown in [35, 36]. Finally, *linear* memory from hyperbolic encounters may also leave an imprint in the LISA band, see e.g. [103]. This low-frequency part of the waveform may be sensitive to the presence of dissipation during the encounter [104, 105]. We leave for future work a more detailed study of this possibility.

Having derived the first realistic estimates of LISA's sensitivity to GW memory, we are convinced that this subtle effect of General Relativity will play a relevant role in the scientific results of future GW missions.

VIII. ACKNOWLEDGMENTS

The authors would like to thank M. Besançon, J. García Bellido, M. Maggiore, A. Petiteau, C. Pitte, and L. Magaña Zertuche for their precious insight and the

fruitful discussions we had during this project. The authors acknowledge E. Barausse for his help regarding MBHB population models and catalogs, which were critical inputs for this work. The authors also thank the LISA Simulation Working Group and the LISA Simulation Expert Group for the lively discussions on all simulation-related activities.

The research leading to these results has received funding from the Spanish Ministry of Science and Innovation (PID2020-115845GB-I00/AEI/10.13039/501100011033). IFAE is partially funded by the CERCA program of the Generalitat de Catalunya. SG has the support of the predoctoral program AGAUR FI SDUR 2022 from the Departament de Recerca i Universitats from Generalitat de Catalunya and the European Social Plus Fund. D. Blas acknowledges the support from the Departament de Recerca i Universitats from Generalitat de Catalunya to the Grup de Recerca 00649 (Codi: 2021 SGR 00649).

LH would like to acknowledge financial support from the European Research Council (ERC) under the European Union Horizon 2020 research and innovation programme grant agreement No 801781. LH further acknowledges support from the Deutsche Forschungsgemeinschaft (DFG, German Research Foundation) under Germany's Excellence Strategy EXC 2181/1 - 390900948 (the Heidelberg STRUCTURES Excellence Cluster). The authors thank the Heidelberg STRUCTURES Excellence Cluster for financial support.

ST is supported by the Swiss National Science Foundation (SNSF) Ambizione Grant Number: PZ00P2-202204.

JZ is supported by the Swiss National Science Foundation (SNSF) through a Postdoc.Mobility Fellowship (Grant No. P500PT-222346).

Computations were performed on the DANTE platform, APC, France.

Appendix A: Details on the definition and modeling of memory

In this appendix, we provide useful details on the practical evaluation of Eq. (1), as well as its use for a viable definition of memory to claim a detection of the phenomenon.

a. *Memory in the* $(2,0)$ *mode*

The claim that non-linear memory of non-precessing and non-eccentric binary black hole coalescence's is predominantly found in the $(2,0)$ mode follows directly from its formula in terms of a spin-weighted mode decomposition by explicitly evaluating the angular integral within Eq. (1). Such an analytic computation of the angular integral is rendered possible through a translation of the TT projected factor into spherical harmonics as for instance shown in paragraph IV (C) of Ref. [35], resulting in the explicit formula [20, 24]

$$h^{\ell m}_{mem} = \frac{R}{c} \sum_{\ell',\ell''\geq 2} \sum_{m',m''} \Gamma^{l'm'm''l''}_{lm} \int_{-\infty}^{u} \mathrm{d}u' \langle \dot{h}^{\ell' m'}_0 \dot{h}^{*\ell'' m''}_0 \rangle, \tag{A1}$$

with

$$\Gamma^{l'm'm''l''}_{lm} \equiv (-1)^{m+m''} \sqrt{\frac{(l-2)!}{(l+2)!}} \sqrt{\frac{(2l'+1)(2l''+1)(2l+1)}{4\pi}} \begin{pmatrix} l' & l'' & l \\ m' & -m'' & -m \end{pmatrix} \begin{pmatrix} l' & l'' & l \\ 2 & -2 & 0 \end{pmatrix}, \tag{A2}$$

where the big parenthesis represent $3-j$ symbols, which in this case are only non zero if $m = m' - m''$ and $|l' - l''| \leq l \leq l' + l''$.

While Eq. (A1) provides the formula for the memory modes with the least amount of numerical computation needed, it is equivalent to the output of the publicly available and numerically optimized `GWMemory` package [78], as both correspond to a spin-weighted expansion of Eq. (1).

From the selection rule above it becomes evident that for a quasi-circular and non-precessing signal, for which most of the energy in GWs is released into the $(2,2)$ mode of the primary wave, the memory is predominantly found in the $m = 0$ modes with $2 \leq l \leq 4$. Moreover, compared to the $(2,0)$ memory mode, the $(4,0)$ mode is suppressed by two orders of magnitude while the $(3,0)$ memory mode vanishes entirely due to the symmetry over the orbital plane [24], such that in the end the memory of non-precessing binary black hole coalescence's predominantly appears in the $(2,0)$ mode [32, 48].

To be more precise, the conclusion that all modes other than the $(2,0)$ mode can be disregarded in Eq. (A1) is more complex, since with increasing accuracy also other modes than the $(2,2)$ mode of the primary waves become important. However, due to the presence of the spacetime averaging over the scales of variation of primary waves, this conclusion will not change, as we will further discuss below.

b. *Evaluation of the spacetime averaging*

But first, we want to discuss the implications of the averaging for the dominant $(2,0)$ mode of memory. It turns out that for $m = 0$ modes the average can effectively be dropped in the case of quasi-circular and non-precessing

binaries[5]

To understand this statement it is first necessary to know that for a typical setting relevant for GW detection and after having identified the gauge-invariant contribution to the GW energy-flux, the spacetime average $\langle ... \rangle$ can be reduced to a purely temporal average over orbital time-scales (see Sec. 1.4.3 in [70]). If in addition the integrand in Eq. (1) does not vary significantly over these scales of the primary waves, the average can effectively be disregarded. Notice that this is precisely the case for memory sourced by the primary $(2,2)$ mode only, since the dependence on the orbital phase of the primary modes cancels within the integrand in Eq. (A1) for $m = 0$ modes. Thus, for quasi-circular and non-precessing compact binary coalescence's any explicit spacetime average over orbital scales within the computation of the $(2,0)$ mode of memory through Eq. (A1) can be dropped, as it is common practice in the community.

c. *Definition of memory and claim of detection*

However, one should nevertheless keep in mind that in defining non-linear memory, the average in Eqs. (1) and (A1) is in fact essential. This is because the automatic cancellation of the oscillations on orbital time-scales within the memory modes is only approximate and can not be relied on in general, in particular in the case of eccentric and precessing binaries for instance. Yet, a sharp separation in scales of variation between non-linear memory and the primary waves is important in order to be able to talk about memory as a clearly distinct component of the total radiation that can individually be searched for.

In fact, even for the quasi-circular and non-precessing binaries addressed in the present work, the average is necessary to identify the $(2,0)$ mode as the only relevant mode of the memory signal. This is because with increasing accuracy of detectors it is actually not true that all modes beyond the dominant $(2,2)$ mode of the primary wave can simply be discarded. Indeed, when computing the memory through the `GWMemory` package we ought to consider all the modes available within the `NRHybSur3dq8` surrogate model, as otherwise the resulting memory would be significantly off. This in turn implies that also additional memory modes in Eq. (A1) are present that would contain oscillatory features if the averaging would simply be dropped. What is more, the oscillatory features within these additional modes would actually impact our SNR computations for certain regions of the parameter space. Thus, the modes computed through Eq. (A1) with $m \neq 0$ are only truly insignificant if an explicit averaging is considered that cancels such oscillations on orbital timescales. In other words, the statement that it is sufficient to only compute the $(2,0)$ mode within Eq. (A1) actually necessitates the presence of the space-time averaging. In the case of precessing and eccentric binaries, such a distinction between oscillatory features and memory within Eq. (A1) will be even more pressing, since also the $m \neq 0$ modes will contain non-negligible memory components.

We want to stress, however, that such oscillatory features within the asymptotic radiation that are sourced by the primary waves are not un-physical. In the language of balance laws [12, 41, 52, 106, 107], they belong to the *null* part of the total strain, in contrast to the familiar oscillatory contributions that are sourced by the movement of masses, such as the dominant $(2,2)$ mode or the oscillations within the total $(2,0)$ mode shown in Fig. 1 associated to the ring-down of the final black-hole, which represent the *ordinary* part of the radiation. Yet, none of the oscillations on orbital and ring-down time-scales are to be considered as part of the GW displacement memory, regardless whether they appear within the null part or the ordinary part of the waveform.[6]

Indeed, a true measurement of non-linear displacement memory that is associated with the profound theoretical consequences outlined in the introduction[7] requires the claim of detecting its defining property of a permanent distortion of spacetime after the passage of gravitational radiation. However, of course current GW detectors designed to measure changes in relative distance at a restricted frequency band are not capable of measuring such a permanent modification of proper distances but rather have only access to the sharp raise of non-linear memory with a characteristic time scale of the merger, as clearly shown if Fig. 2. In this context, for a claim of detection of memory it is crucial to ensure that the memory signal, which appears as an additional oscillatory feature within the detector response of LISA, can unambiguously be associated to an offset in proper distances between freely falling test masses. Thus, in a search for memory, any oscillatory feature on orbital or ringdown time-scales that are not

[5] See also the discussion in App. C of [74].

[6] It is important to note that strictly speaking, the BMS balance laws do not allow for an isolation of a displacement memory component as an independent entity within the time-varying waveform. The balance-laws only provide an unambiguous identification of the total final offset of memory. A separation into the null and ordinary parts of the total time-dependent strain through the balance laws only provide an approximate isolation of the displacement memory in the case of non-precessing and non-eccentric binaries, since in this case almost all the memory is excursively present within the null part of the asymptotic radiation, while the oscillations on orbital and ring-down time-scales are mostly found in the ordinary piece. In more general cases, an averaging procedure would however be inevitable to isolate a time-dependent non-linear memory signal (see also App. C in [35]).

[7] In particular, GW memory provides an empirical window into fascinating questions on fundamental physics through its relation to asymptotic symmetries as well as the soft theorems of scattering theory.

associated with the raise of displacement memory, need to be disregarded by demanding a sharp separation in scales of variation between memory and the primary waves. This is precisely ensured through an explicit averaging within Eqs. (1) and (A1).

Appendix B: TDI memory response in the long wavelength limit

In this section, we want to provide a brief analytical understanding of why the TDI output of the memory signal in Figure 2 looks like a burst-like event compared to the naively expected step-like function. For this, we need to understand how the TDI X variables are related to the original GW strain h. This is given by a complicated combination of the single-link data streams shifted by several delay operators, as given in Eq. (9). In the low-frequency limit $\omega L \ll 1$, i.e. for frequencies ω much smaller than the inverse of the detector arm L, one can show the following relationship between the output of the first generation TDI combination $X_{1.5}$ and the GW strain h (see Eq. (51) of Ref. [91])

$$X_{1.5} \approx 2L^2(\epsilon^a_{12}\epsilon^b_{12} - \epsilon^a_{13}\epsilon^b_{13})\partial_t^2 h_{ab}, \tag{B1}$$

where ϵ_{ij} is the unit vector from spacecraft j towards spacecraft i. The second generation of TDI combination X_2 is related to the first generation by

$$|X_2| = 2\sin(2\omega L)|X_{1.5}| \tag{B2}$$

so, in the low-frequency limit $|X_2| \approx 4\omega L|X_{1.5}|$, and we recognize that in frequency space this is simply the derivative of $X_{1.5}$. Therefore, X_2 is proportional to an additional derivative of the strain $X_2 \propto \partial_t^3 h$.

Going back to the step-like behavior of the memory signal, this can be approximated by a hyperbolic function with time raise $\Delta T = 60 M_{tot}$, as explained in Section II,

$$h(t) = \tanh\left(\frac{2\pi(t-t_c)}{\Delta T}\right), \tag{B3}$$

with t_c the merger time. We show this function in Figure 12 with its higher derivatives up to the third, noting that they all go to zero sufficiently far from the merger. In particular, note how the third derivative (red line) resembles the TDI result of the memory signal shown in Figure 2.

Appendix C: Comparison of the memory between Surrogate_CCE and GWMemory package

As mentioned in the main text, we found some differences between the GW memory computed through Eq. (5), which subtracts the (2,0) mode of NRHybSur3dq8_CCE to that of NRHybSur3dq8_CCE, and through Eq. (1) from the NRHybSur3dq8 waveforms using the GWMemory package. The two differ by some

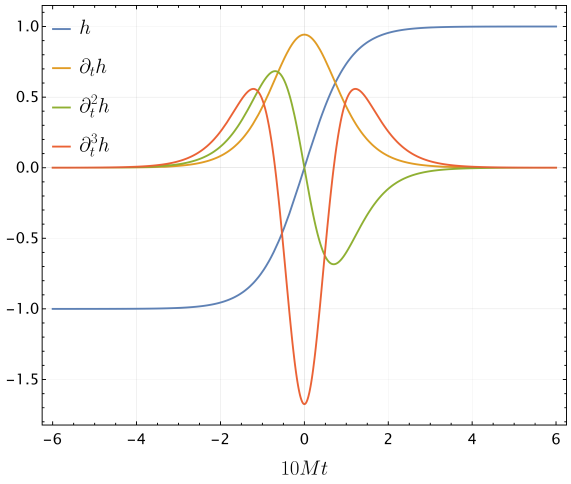

Figure 12. Visualisation of the step-like behaviour of the memory approximated by the hyperbolic tangent, Eq. (B3), and its first, second and third derivatives. We take $t_c = 0$ and $\Delta T = 60 M_{tot}$ as explained in the main text.

oscillating features present in the first method compared to the second, as can be seen in Figure 13, where the smooth blue curve is the TDI of the memory calculated through the GWMemory package, while the red curve is calculated through Eq. (5). These oscillations are visible as small peaks in the power spectra of the signals shown in Figure 14, at frequencies higher than the typical frequencies of the memory. By comparing them with Figure 3 in the main text, one can see that they are just below the maximum frequency of the (2,2) mode of the primary signal. This might suggest that the discrepancy between the two has a physical origin that is better captured in the NR simulations. However, as mentioned in the text, the two waveforms used in Eq. (5) are not constructed exactly in the same way, then the comparison in Eq. (5) might not be robust in general, and can give rise to some numerical error, such as residual coming from the ringdown.

While rather small in the strain time-series (see left-hand side of 14), these high-frequency features are significantly magnified by the LISA response function, acting as a third-order high-pass filter (see right-hand plot of Figure 13). We find, however, that these discrepancies do not impact sensibly SNR prospects for equal-mass sources, but have a stronger impact for higher q as visible in Figure 15.

In Figure 15, we present the SNR as a function of (q, M_{tot}) for the memory computed through the GWMemory package, and we underlay in dashed lines the computation using Eq. (5). The discrepancy between the memory SNR calculated with these two methods becomes obvious in this plot. In particular, we found a strange bump appearing at masses $M_{tot} \gtrsim 10^6 M_\odot$ and high mass ratio when the memory is computed with Eq. (5). Again, we believe this is due to the two waveforms NRHybSur3dq8_CCE and NRHybSur3dq8 not being

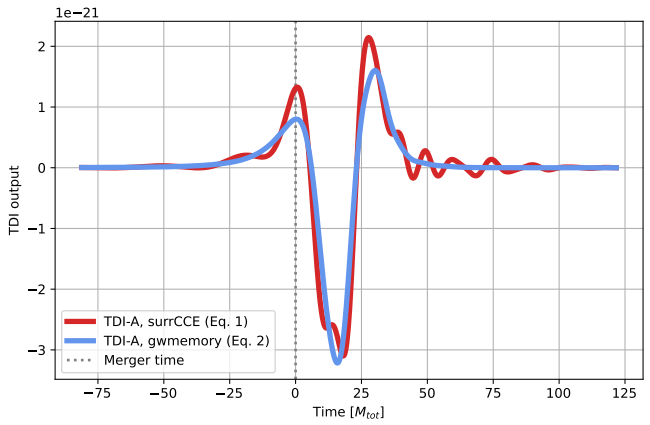

Figure 13. Comparison of the TDI-A response for the same source of Figure 3, for the memory computed through Eq.(5) (red) and the `GWMemory` package estimate from the `NRHybSur3dq8` waveforms (blue).

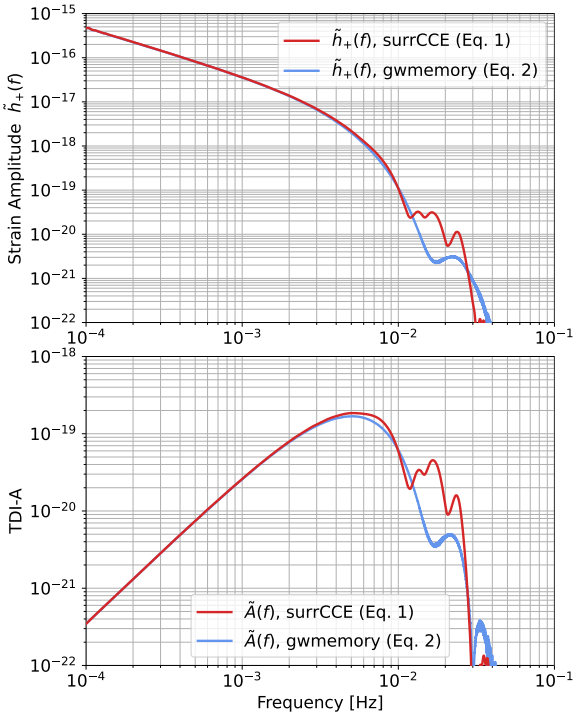

Figure 14. As in Figure 13 for the comparison of the strain amplitude and TDI-A response, here in the frequency domain. In the first method, the FT of the memory presents additional peaks at high frequencies, about the peak frequency of the (2,2) mode of the primary signal. At the level of computing the SNR, for this source, the mismatch between these two waveforms is smaller than $\mathcal{O}(1)$, thus not affecting the prediction on detectability.

calculated in the same way, with same gauge fixing strategies [13], so that the two are not directly comparable in general. As a consequence, the subtraction of the two can leave a substantial residual at high frequencies, more pronounced for higher mass-ratio, and with brighter signatures through LISA response for higher total masses. However, this difference may also (partially) have a physical origin, as NR waveforms return slightly higher memory and high-frequency features in the merger/ringdown.

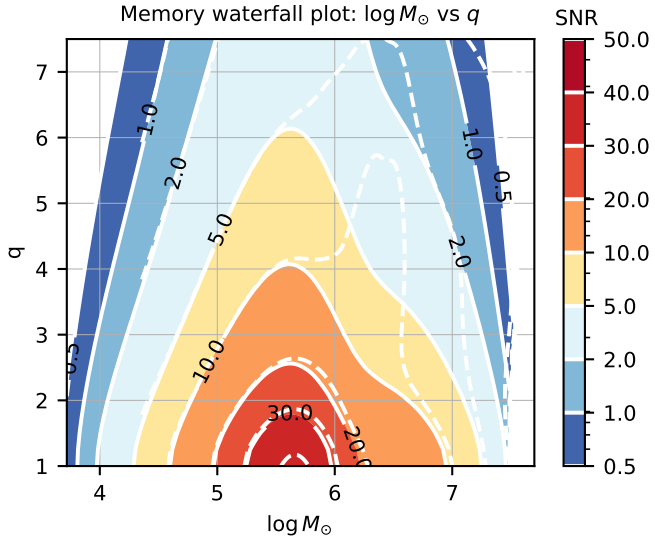

Figure 15. Study of the q-dependence of the memory SNR, using the baseline 2 in Table I (apart from q obviously variable here). We are comparing the SNR computed using `GWMemory` [108] (color-filled and plain-line contours) and Eq. (5) (dashed-line contours). We have noticed an excess of signal when computing memory from CCE surrogate waveforms and Eq. (5) given by the bump visible at masses $M_{tot} \gtrsim 10^6 M_\odot$ and high mass ratio. On the lower panel, we draw the evolution of the SNR for a set of system total masses as the mass ratio q increases and we compare it with the scaling $\sim [4q/(1+q)^2]^\alpha$ with $1 \leq \alpha \leq 2.5$, where the $\alpha = 1$ is the Post-Newtonian expectation and $\alpha = 1.65$ was found in Ref. [98].

[1] Y. B. Zel'dovich and A. G. Polnarev, Sov. Astron. **18**, 17 (1974).
[2] V. B. Braginsky and L. P. Grishchuk, Sov. Phys. JETP **62**, 427 (1985).
[3] V. B. Braginsky and K. S. Thorne, Nature (London) **327**, 123 (1987).
[4] D. Christodoulou, Phys. Rev. Lett. **67**, 1486 (1991).
[5] E. E. Flanagan, A. M. Grant, A. I. Harte, and D. A. Nichols, Phys. Rev. D **99**, 084044 (2019).
[6] A. M. Grant and D. A. Nichols, Phys. Rev. D **105**, 024056 (2022), [Erratum: Phys.Rev.D 107, 109902 (2023)].
[7] A. M. Grant and D. A. Nichols, Phys. Rev. D **107**, 064056 (2023), [Erratum: Phys.Rev.D 108, 029901 (2023)].
[8] S. Siddhant, A. M. Grant, and D. A. Nichols, (2024).
[9] S. Pasterski, A. Strominger, and A. Zhiboedov, JHEP **12**, 053 (2016).
[10] D. A. Nichols, Phys. Rev. D **98**, 064032 (2018).
[11] A. Strominger and A. Zhiboedov, JHEP **01**, 086 (2016).
[12] A. Ashtekar, T. De Lorenzo, and N. Khera, Gen. Rel. Grav. **52**, 107 (2020).
[13] K. Mitman *et al.*, (2024).
[14] A. Strominger, *Lectures on the Infrared Structure of Gravity and Gauge Theory* (2017).
[15] L. Bieri and D. Garfinkle, Phys. Rev. D **89**, 084039 (2014), arXiv:1312.6871 [gr-qc].
[16] L. Bieri and A. Polnarev, Class. Quant. Grav. **41**, 135012 (2024), arXiv:2402.02594 [gr-qc].
[17] A. G. Wiseman and C. M. Will, Phys. Rev. D **44**, R2945 (1991).
[18] L. Blanchet and T. Damour, Phys. Rev. D **46**, 4304 (1992).
[19] K. S. Thorne, Phys. Rev. D **45**, 520 (1992).
[20] M. Favata, Phys. Rev. D **80**, 024002 (2009).
[21] L. Blanchet, G. Faye, B. R. Iyer, and S. Sinha, Class. Quant. Grav. **25**, 165003 (2008), [Erratum: Class.Quant.Grav. 29, 239501 (2012)].
[22] M. Favata, Class. Quantum Gravity **27**, 084036 (2010).
[23] D. Garfinkle, Class. Quant. Grav. **39**, 135010 (2022), arXiv:2201.05543 [gr-qc].
[24] J. Zosso, *Probing Gravity - Fundamental Aspects of Metric Theories and their Implications for Tests of General Relativity*, Ph.D. thesis, Zurich, ETH (2024), arXiv:2412.06043 [gr-qc].
[25] M. Favata, The Astrophysical Journal **696**, L159 (2009), publisher: American Astronomical Society.
[26] S. Gasparotto, R. Vicente, D. Blas, A. C. Jenkins, and E. Barausse, Physical Review D **107**, 124033 (2023), publisher: American Physical Society.
[27] Y. Xu, M. Rosselló-Sastre, S. Tiwari, M. Ebersold, E. Z. Hamilton, C. García-Quirós, H. Estellés, and S. Husa, (2024).
[28] S. Tiwari, M. Ebersold, and E. Z. Hamilton, Phys. Rev. D **104**, 123024 (2021).
[29] D. Lopez, S. Tiwari, and M. Ebersold, Phys. Rev. D **109**, 043039 (2024).
[30] B. Goncharov, L. Donnay, and J. Harms, (2023).
[31] L. Heisenberg, Philosophical Transactions of the Royal Society A: Mathematical, Physical and Engineering Sciences **382**, 20230086 (2023), publisher: Royal Society.
[32] F. D'Ambrosio, F. Gozzini, L. Heisenberg, H. Inchauspé, D. Maibach, and J. Zosso, "Testing gravitational waveforms in full General Relativity," (2024), arXiv:2402.19397 null.
[33] S. M. Du and A. Nishizawa, Phys. Rev. D **94**, 104063 (2016).
[34] S. Tahura, D. A. Nichols, and K. Yagi, Phys. Rev. D **104**, 104010 (2021).
[35] L. Heisenberg, N. Yunes, and J. Zosso, Phys. Rev. D **108**, 024010 (2023).
[36] L. Heisenberg, G. Xu, and J. Zosso, JCAP **05**, 119 (2024), arXiv:2401.05936 [gr-qc].
[37] L. O. McNeill, E. Thrane, and P. D. Lasky, Phys. Rev. Lett. **118**, 181103 (2017).
[38] S. Ghosh, A. Weaver, J. Sanjuan, P. Fulda, and G. Mueller, Phys. Rev. D **107**, 084051 (2023).
[39] M. Hübner, C. Talbot, P. D. Lasky, and E. Thrane, Phys. Rev. D **101**, 023011 (2020).
[40] M. Ebersold and S. Tiwari, Phys. Rev. D **101**, 104041 (2020).
[41] Z.-C. Zhao, X. Liu, Z. Cao, and X. He, Phys. Rev. D **104**, 064056 (2021).
[42] M. Hübner, P. Lasky, and E. Thrane, Phys. Rev. D **104**, 023004 (2021).
[43] N. Seto, Mon. Not. Roy. Astron. Soc. **400**, L38 (2009).
[44] J. M. Cordes and F. A. Jenet, Astrophys. J. **752**, 54 (2012).
[45] G. Agazie *et al.*, Astrophys. J. **963**, 61 (2024).
[46] M. Punturo *et al.*, Class. Quant. Grav. **27**, 194002 (2010).
[47] D. Reitze *et al.*, Bull. Am. Astron. Soc. **51**, 035 (2019).
[48] M. Favata, Astrophys. J. Lett. **696**, L159 (2009).
[49] A. D. Johnson, S. J. Kapadia, A. Osborne, A. Hixon, and D. Kennefick, Phys. Rev. D **99**, 044045 (2019).
[50] K. Islo, J. Simon, S. Burke-Spolaor, and X. Siemens, (2019).
[51] T. Islam, S. E. Field, G. Khanna, and N. Warburton, (2021).
[52] S. Sun, C. Shi, J.-d. Zhang, and J. Mei, Phys. Rev. D **107**, 044023 (2023), arXiv:2207.13009 [gr-qc].
[53] S. Sun, C. Shi, J.-d. Zhang, and J. Mei, Phys. Rev. D **110**, 024050 (2024), arXiv:2401.11416 [gr-qc].
[54] R. van Haasteren and Y. Levin, Mon. Not. Roy. Astron. Soc. **401**, 2372 (2010).
[55] G. Janssen *et al.*, PoS **AASKA14**, 037 (2015).
[56] V. Varma, S. E. Field, M. A. Scheel, J. Blackman, L. E. Kidder, and H. P. Pfeiffer, Physical Review D **99**, 064045 (2019), publisher: American Physical Society.
[57] J. Yoo, K. Mitman, V. Varma, M. Boyle, S. E. Field, N. Deppe, F. Hébert, L. E. Kidder, J. Moxon, H. P. Pfeiffer, M. A. Scheel, L. C. Stein, S. A. Teukolsky, W. Throwe, and N. L. Vu, Physical Review D **108**, 064027 (2023), publisher: American Physical Society.
[58] E. Barausse and A. Lapi, "Massive Black-Hole Mergers," (2021) arXiv:2011.01994 [astro-ph.GA].
[59] E. Barausse, I. Dvorkin, M. Tremmel, M. Volonteri, and M. Bonetti, Astrophys. J. **904**, 16 (2020).
[60] E. Barausse, Mon. Not. Roy. Astron. Soc. **423**, 2533 (2012).
[61] A. Sesana, E. Barausse, M. Dotti, and E. M. Rossi, Astrophys. J. **794**, 104 (2014).

[62] F. Antonini, E. Barausse, and J. Silk, Astrophys. J. **812**, 72 (2015).
[63] M. Colpi *et al.*, "LISA Definition Study Report," (2024), arXiv:2402.07571 [astro-ph, physics:gr-qc].
[64] J.-B. Bayle, Q. Baghi, A. Renzini, and M. Le Jeune, "LISA GW Response," (2023), language: eng.
[65] J.-B. Bayle, A. Hees, M. Lilley, and C. Le Poncin-Lafitte, "LISA Orbits," (2022), language: eng.
[66] J.-B. Bayle and O. Hartwig, Physical Review D **107**, 083019 (2023), publisher: American Physical Society.
[67] J.-B. Bayle, O. Hartwig, and M. Staab, "LISA Instrument," (2023).
[68] M. Staab, J.-B. Bayle, and O. Hartwig, "PyTDI," (2023), language: eng.
[69] M. Favata, Journal of Physics: Conference Series **154**, 012043 (2009).
[70] M. Maggiore, *Gravitational Waves: Volume 1: Theory and Experiments* (Oxford University Press, 2007).
[71] E. Barausse, V. Morozova, and L. Rezzolla, Astrophys. J. **758**, 63 (2012), [Erratum: Astrophys.J. 786, 76 (2014)], arXiv:1206.3803 [gr-qc].
[72] R. Arnowitt, S. Deser, and C. W. Misner, Phys. Rev. **121**, 1556 (1961).
[73] R. A. Isaacson, Phys. Rev. **166**, 1272 (1968).
[74] M. Favata, Phys. Rev. D **84**, 124013 (2011), arXiv:1108.3121 [gr-qc].
[75] R. A. Isaacson, Phys. Rev. **166**, 1263 (1968).
[76] R. A. Isaacson, Phys. Rev. **166**, 1272 (1968).
[77] F. D'Ambrosio, S. D. B. Fell, L. Heisenberg, D. Maibach, S. Zentarra, and J. Zosso, (2022), arXiv:2201.11634 [gr-qc].
[78] C. Talbot, E. Thrane, P. D. Lasky, and F. Lin, Phys. Rev. D **98**, 064031 (2018).
[79] K. Mitman, J. Moxon, M. A. Scheel, S. A. Teukolsky, M. Boyle, N. Deppe, L. E. Kidder, and W. Throwe, Phys. Rev. D **102**, 104007 (2020).
[80] M. Rosselló-Sastre, S. Husa, and S. Bera, (2024).
[81] M. Vallisneri, Physical Review D **72**, 042003 (2005), publisher: American Physical Society.
[82] Q. Baghi, N. Karnesis, J.-B. Bayle, M. Besançon, and H. Inchauspé, Journal of Cosmology and Astroparticle Physics **2023**, 066 (2023), publisher: IOP Publishing.
[83] L. Heisenberg, H. Inchauspé, D. Q. Nam, O. Sauter, R. Waibel, and P. Wass, Physical Review D **108**, 122007 (2023), publisher: American Physical Society.
[84] M. Tinto and S. V. Dhurandhar, Living Reviews in Relativity **24**, 1 (2020).
[85] L. S. S. Team, *Science Requirement Document*, Tech. Rep. ESA-L3-EST-SCI-RS-001 (2018).
[86] S. Babak, M. Hewitson, and A. Petiteau, "LISA Sensitivity and SNR Calculations," (2021), arXiv:2108.01167 [astro-ph, physics:gr-qc].
[87] M. Boyle *et al.*, Classical and Quantum Gravity **36**, 195006 (2019), publisher: IOP Publishing.
[88] D. J. A. McKechan, C. Robinson, and B. S. Sathyaprakash, Classical and Quantum Gravity **27**, 084020 (2010).
[89] D. Quang Nam, J. Martino, Y. Lemière, A. Petiteau, J.-B. Bayle, O. Hartwig, and M. Staab, Physical Review D **108**, 082004 (2023), publisher: American Physical Society.
[90] C. Pitte, Q. Baghi, S. Marsat, M. Besançon, and A. Petiteau, Physical Review D **108**, 044053 (2023), publisher: American Physical Society.
[91] S. Babak, A. Petiteau, and M. Hewitson, (2021).
[92] A. Buonanno, G. B. Cook, and F. Pretorius, Phys. Rev. D **75**, 124018 (2007).
[93] Y. Chen *et al.*, (2024).
[94] A. Zonca, L. P. Singer, D. Lenz, M. Reinecke, C. Rosset, E. Hivon, and K. M. Gorski, Journal of Open Source Software **4**, 1298 (2019).
[95] T. Robson, N. J. Cornish, and C. Liu, Class. Quant. Grav. **36**, 105011 (2019), arXiv:1803.01944 [astro-ph.HE].
[96] K. M. Górski, E. Hivon, A. J. Banday, B. D. Wandelt, F. K. Hansen, M. Reinecke, and M. Bartelmann, The Astrophysical Journal **622**, 759 (2005), publisher: IOP Publishing.
[97] C. Pitte, Q. Baghi, S. Marsat, M. Besançon, and A. Petiteau, Phys. Rev. D **108**, 044053 (2023).
[98] X. Liu, X. He, and Z. Cao, Phys. Rev. D **103**, 043005 (2021).
[99] Z. Cao and W.-B. Han, Classical and Quantum Gravity **33**, 155011 (2016).
[100] D. Pollney and C. Reisswig, Astrophys. J. Lett. **732**, L13 (2011).
[101] E. Barausse, K. Dey, M. Crisostomi, A. Panayada, S. Marsat, and S. Basak, Phys. Rev. D **108**, 103034 (2023).
[102] C. García-Quirós, M. Colleoni, S. Husa, H. Estellés, G. Pratten, A. Ramos-Buades, M. Mateu-Lucena, and R. Jaume, Physical Review D **102**, 064002 (2020), publisher: American Physical Society.
[103] M. Caldarola, S. Kuroyanagi, S. Nesseris, and J. Garcia-Bellido, Phys. Rev. D **109**, 064001 (2024).
[104] M. Gröbner, W. Ishibashi, S. Tiwari, M. Haney, and P. Jetzer, Astron. Astrophys. **638**, A119 (2020), arXiv:2005.03571 [astro-ph.GA].
[105] S. Dandapat, M. Ebersold, A. Susobhanan, P. Rana, A. Gopakumar, S. Tiwari, M. Haney, H. M. Lee, and N. Kolhe, Phys. Rev. D **108**, 024013 (2023), arXiv:2305.19318 [gr-qc].
[106] N. Khera, B. Krishnan, A. Ashtekar, and T. De Lorenzo, Phys. Rev. D **103**, 044012 (2021).
[107] K. Mitman *et al.*, Phys. Rev. D **103**, 024031 (2021).
[108] C. Talbot, E. Thrane, P. D. Lasky, and F. Lin, Physical Review D **98**, 064031 (2018), publisher: American Physical Society.